Chapter 4

STRAIN ENGINEERING OF $SrTiO_3$

Roger Wördenweber[1,*] and Yang Dai[2]

[1]Institute of Complex Systems – Bioelectronics (ICS-8),
Forschungszentrum Jülich, Jülich, Germany
[2]Shenzhen Institutes of Advanced Technology,
Chinese Academy of Sciences, Shenzhen, China

ABSTRACT

Due to their tendency to form ionic states, transition metal oxides and especially $SrTiO_3$ exhibit extraordinary ferroelectric properties. However, they typically exhibit these extraordinary properties close to the ferroelectric phase transition temperature, which usually deviates significantly from room temperature. The question arises as to whether, and how, these extraordinary properties can be utilized. It is therefore of major interest to engineer these materials to fully exploit and understand their potential, and to make them suitable or more suitable for various applications.

One method of engineering the properties of these materials is to use mechanical strain. In particular, epitaxial strain, which is automatically

* Corresponding Author Email: r.woerdenweber@fz-juelich.de.

generated in epitaxial films grown on lattice-mismatched substrates, allows crystalline oxides to be elastically strained up to percent levels. Under such strain, the properties of the transition metal oxides can be altered significantly.

In this chapter, we review the use of epitaxial strain to modify the ferroelectric, electronic, and structural properties of $SrTiO_3$. We discuss how the ferroelectric properties can be tuned systematically by strain. This includes the tuning of the ferroelectric transition temperature, permittivity, and the type of ferroelectricity. We demonstrate that these epitaxially strained films typically represent textbook-like relaxor ferroelectrics and are highly tunable. Furthermore, we show that even the conductance of the nominally insulating material can be modified by epitaxial strain. With adequate strain, $SrTiO_3$ not only becomes semiconductor-like, it also exhibits an "electronic plasticity," which is of interest for applications ranging from memristor to neuromorphic devices such as artificial synapses (e-synapses). The examples discussed demonstrate how elastic epitaxial strain represents an exciting option for engineering and fine-tuning the properties of $SrTiO_3$ thin films.

Keywords: strain, epitaxial film, phase transition, relaxor, conductance

1. INTRODUCTION

The development of modern electronic devices has revolutionized the quality and way of life over the past few decades. In particular, the development of thin-film technology has enabled the size of electronic devices to be reduced while also enhancing their performance significantly. Electronic components work faster (modern computers operate at several GHz), are much smaller (thin-film transistors are now just a few nm in size), and can be integrated into complex electronics. This development was brought about not only by improvements in thin-film deposition, lithography, and processing techniques, but also the exchange and optimization of the properties of the different material components involved. The latter aspect is crucial to the further development of electronic devices. Research and concepts to improve material properties therefore represent a vital issue in the field of electronics.

Metal oxides are a family of materials that are widely used in the production of advanced electronic devices. Not only are they used as dielectric layers in transistors (simple field-effect transistor to complementary metal-oxide-semiconductor) or ferroelectric switches in memory devices (ferroelectric random-access memory or dynamic random-access memory), but there have been recent reports of prototype applications such as ultrafast switching, magnetic field detectors, piezoelectric nanotubes for microfluidic systems, electrocaloric coolers, phased-array radar, three-dimensional trench capacitors for dynamic random access memories, and even neuromorphic electronic components based on metal oxides [3, 4]. Depending on the type of application, a further miniaturization or improvement of device performance would require a further improvement of the ferroelectric properties of these materials. For a number of applications, this would require, for instance, a higher dielectric permittivity [5]. For example, the gate dielectric SiO_2 ($\varepsilon \approx 3.9$) of classical transistors has previously been substituted by HfO_2 ($\varepsilon \approx 25$ [1]). However, there are other candidates with an even higher dielectric permittivity (see Figure 1). For example, TiO_2 already has a permittivity of ~80 [1] and a number of the perovskites ($SrTiO_3$, $BaTiO_3$, and $NaNbO_3$ are shown in Figure 1a) have a permittivity of several hundred at room temperature [6]. In addition to searching for alternative materials for specific applications, there are other ways of improving the performance of existing materials. The perovskites shown in Figure 1a exhibit a larger permittivity at the phase transition temperature T_o compared to room temperature (see also Figure 2). In particular, $SrTiO_3$ has an extremely high dielectric permittivity of ~25,000 at T_o.

Unfortunately, the transition temperature of these perovskites deviates considerably from room temperature. For $SrTiO_3$, it is far below room temperature, and in nearly all other cases, it is far above room temperature (see Figure 1b). The classical way of modifying T_o (and thus all other ferroelectric properties, including permittivity) is given by substituting the elements. In the case of $SrTiO_3$, substituting Sr with Ba automatically leads to a near-linear increase of T_o from 0 K for $SrTiO_3$ to ~393 K for $BaTiO_3$ (see Figure 1b). However, this substitution causes a reduction of the

permittivity at T_o. Moreover, for the intermediate stoichiometric regime, larger losses and other disadvantages are expected due to the structural mismatch between both perovskites and the resulting defect formation.

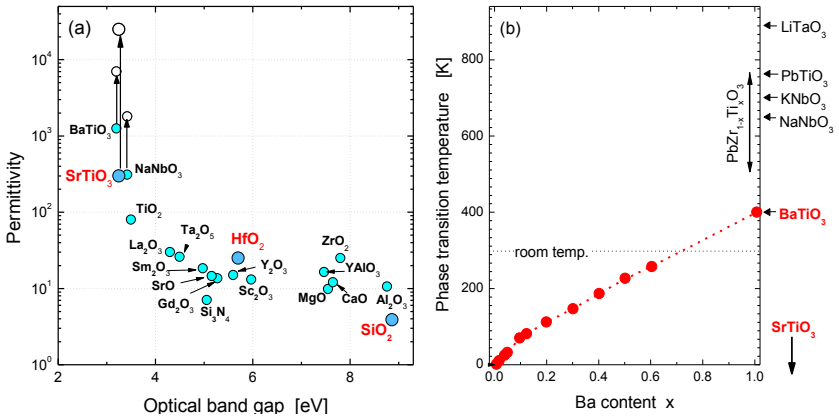

Figure 1. (a) Dielectric permittivity as a function of the optical band gap for various oxides at room temperature (solid symbols) [1]. For the high-k material, the maximum permittivity (open symbols) is added. Please note that the maximum permittivity is typically achieved at the ferroelectric transition temperature. (b) Ferroelectric phase transition temperature T_o for $(Sr_{1-x}Ba_x)TiO_3$ [2]. On the right-hand side, transition temperatures for various perovskites are indicated.

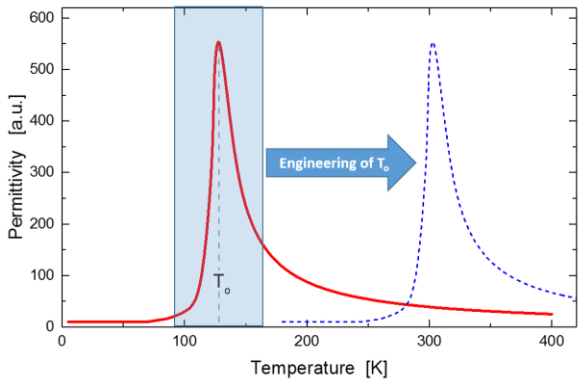

Figure 2. Schematic plot of the typical temperature dependence of the permittivity of a conventional ferroelectric material. The optimal regime for most applications appears to be at the phase transition T_o. In order to utilize these properties, T_o must be shifted to room temperature, as indicated in this figure.

Another way of modifying T_o is the application of mechanical stress. The effect of hydrostatic pressure on the transition temperature of Rochelle salt was demonstrated in the 1930s [8]. However, the hydrostatic pressure and resulting modification of T_o were relatively small. Later in the 1950s, biaxial epitaxial strain, in which a thin film is epitaxially clamped to a substrate but is free to expand in the out-of-plane direction, was shown to alter the ferroelectric transition temperature [9].

In recent years, the magnitude of the biaxial strain that can be imparted has enhanced dramatically. While bulk ferroelectric oxides are brittle and crack under moderate strains (typically at ~0.1%), strains of up to ±3% are today common in epitaxial oxide films. This epitaxial strain is generated simply by the mismatch of the crystalline structure of the film and substrate (see Figure 3). A large mismatch leads to a large strain in the film. Strain ultimately leading to crack formation can also be generated.

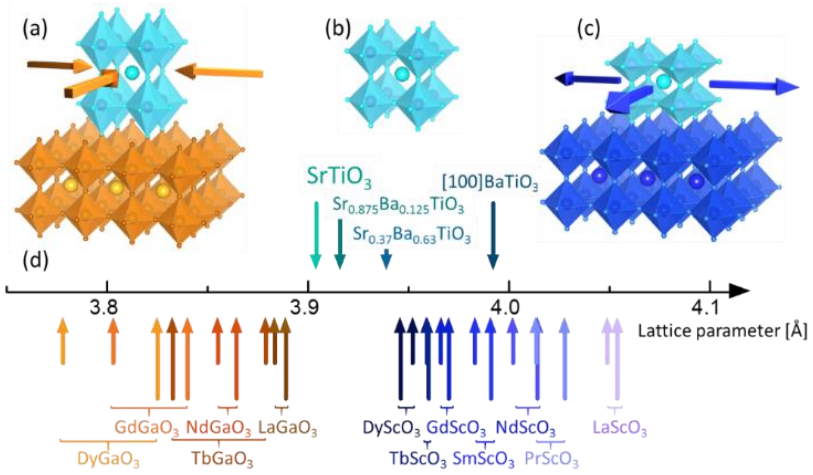

Figure 3. Schematic view of epitaxially strained (Sr,Ba)TiO_3 films on various substrates showing cases of (a) compressive-strained, (b) unstrained, and (c) tensile-strained films depending on the choice of the combination of film composition and substrate. The images were produced using the VESTA program [7]. (d) shows the respective lattice constants of (Sr,Ba)TiO_3 and examples of perovskite substrates (various gallates and scandates). The shorter arrows for the substrates mark the [001] orientation, whereas the longer arrows refer to the [1$\underline{1}$0] orientation.

The epitaxial strain (typically <3%) provides a potentially disorder-free route to achieve large biaxial (in-plane) strain. It has been used to enhance electron mobility in transistors [10], increase catalytic activities [11], alter the electronic band structure [12], modify conductivity to obtain neuromorphic behaviour [13], and significantly increase the superconducting [14], ferromagnetic [15-17], or ferroelectric [18-24] transition temperature. In this chapter, we use and review the epitaxial strain approach. Discussion is restricted to one of the most promising systems, $SrTiO_3$ (partially substituting Sr with Ba), and focuses on the engineering of the ferroelectric properties and the conductivity of epitaxially strained thin $SrTiO_3$ films.

2. WHAT NEEDS TO BE KNOWN ABOUT $SrTiO_3$

Strontium titanate ($SrTiO_3$) is an extremely versatile material. Firstly, although stoichiometric $SrTiO_3$ is an insulator with a band gap of 3.2 eV [25], it has interesting conduction properties. Due to its significant ionic and electronic conduction, $SrTiO_3$ can be used as a mixed ion-electron conductor (MIEC), as can a few other oxides (e.g., TiO_2, CeO_2, $LiFePO_4$, or $LiMnPO_4$) [26]. This mixed conduction allows for the transport of a formally neutral species in a solid (e.g., oxygen in $SrTiO_3$) and is a prerequisite for many interesting kinetic phenomena. One such phenomenon (neuromorphic behaviour) is illustrated in section 5 of this chapter.

Secondly, $SrTiO_3$ is a very promising *high-k* material – a dielectric material with an extremely high permittivity (see Figure 1a and Figure 4). The dielectric permittivity (its real part) ε_r of $SrTiO_3$ is higher than that of most other common ceramic and polymer materials. At room temperature, $SrTiO_3$ is a centrosymmetric paraelectric material with a cubic perovskite structure and a permittivity of $\varepsilon_r \approx 300$. Since it follows Curie–Weiss law:

$$\chi = \varepsilon_r - 1 = \frac{C}{T - T_C} \tag{1}$$

where χ, C, and T_C represent the electric susceptibility, Curie constant, and Curie temperature, respectively, the inverse permittivity decreases in an almost linear fashion with decreasing temperature according to $1/\varepsilon_r \cong (T - T_C)/C$ right down to the Curie temperature $T_C \approx$ 30-42 K [27]. As a consequence, ε_r increases significantly with decreasing temperature. Moreover, since $SrTiO_3$ is an incipient ferroelectric, i.e., it shows no ferroelectric phase transition and therefore no peak in the permittivity-vs-temperature plot (see Figure 2) down to the lowest measurable temperatures, this increase is maintained to zero temperature, where a permittivity of up to 25,000 is measured (see Figure 4).

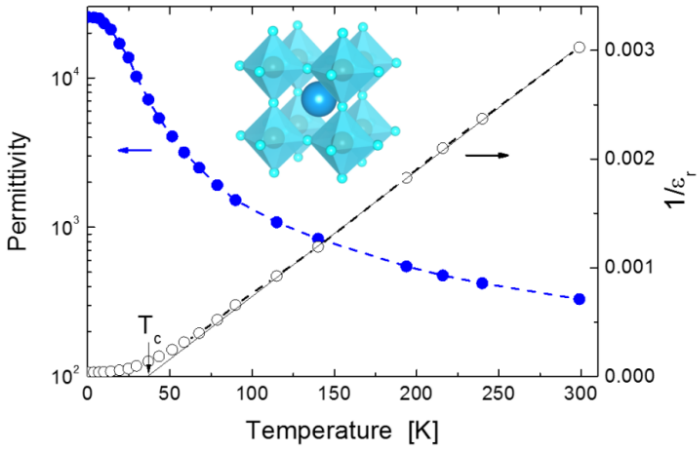

Figure 4. Dielectric response (permittivity ε_r) of $SrTiO_3$ (solid symbols) and inverted permittivity (open symbols), which demonstrate the Curie–Weiss behaviour according to Eq. (1) with a Curie temperature T_C of 30-42 K. The inset outlines the perovskite ABO_3 crystalline structure of $SrTiO_3$ with the face-centred O^{2-} anion octahedron and the cations Sr^{2+} and Ti^{4+} located at the corners (A-site) and centre (B-site) of the unit cell, respectively.

In terms of applications, extremely high permittivity would ideally be utilized by moving the phase transition towards room temperature. This would simultaneously affect (and in most cases improve) the material's other electronic properties at room temperature such as tunability, specific ferroelectric properties, and conductivity. The conventional way of achieving this goal is by substituting Sr with Ba. The resulting mix of $SrTiO_3$

($T_C \approx 35$ K) and $BaTiO_3$ ($T_C \approx 396$ K) [28] leads to a near-linear increase of T_C and therefore phase transition temperature T_o with the amount of Ba (see Figure 1b). The use of strain is another particularly appealing option for thin films. $SrTiO_3$ represents a model system for the examination and use of epitaxial strain. It is the first system which predicted [29] and demonstrated [18-24] a large impact of epitaxial strain on the ferroelectric phase transition. This was the starting point for a series of experiments on the correlation between epitaxial strain and the structural and electronic properties of $SrTiO_3$ [18, 23, 24, 30-34].

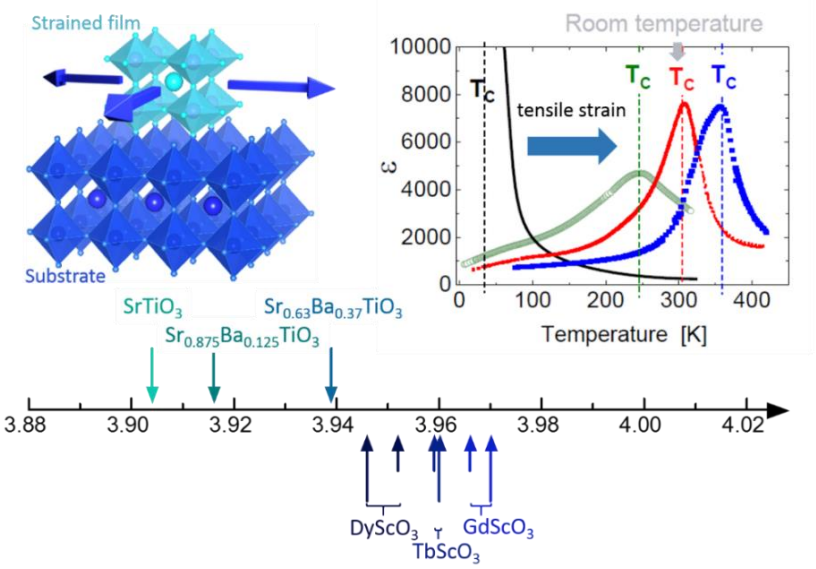

Figure 5. (bottom) Sketch of the nominal lattice mismatch between epitaxial $Sr_{1-x}Ba_xTiO_3$ films (x = 0, 0.125, 0.37) and various (110)-oriented rare-earth scandate substrates. The longer arrows indicate [1$\underline{1}$0] orientation; the shorter arrows depict the [001] orientation of the scandates. (right) Examples of the temperature dependence of the permittivity, demonstrating the shift of T_C towards room temperature. (left) Sketch of the epitaxially tensile-strained film on a lattice mismatched substrate. The surfaces of the substrates have two different lattice parameters. Depending on this, the crystalline orientations cause a large or small strain direction in the epitaxial film.

3. ENGINEERING FERROELECTRIC PROPERTIES BY STRAIN

In this section, we discuss the impact of strain (in-plane tensile strain) on the structure, defect formation, and ferroelectric phase transition of $SrTiO_3$. To enlarge the strain regime, (i) various rare-earth scandates ((110)-oriented $DyScO_3$, $TbScO_3$, and $GdScO_3$) are used as substrates and (ii) in some cases Sr is partially substituted with Ba. The resulting lattice mismatch between the epitaxially grown film and substrate is illustrated in Figure 5. It ranges from 0.16% ($Sr_{0.63}Ba_{0.37}TiO_3$ on $DyScO_3$) to 1.72% ($SrTiO_3$ on $GdScO_3$). Furthermore, to obtain a reliable measure for the shift of the phase transition temperature (T_o is typically close to the maximum of the permittivity), the shift of the Curie–Weiss temperature T_C is used in this analysis. This section is based on the results and discussion presented in Ref. [24].

3.1. Experimental Techniques and Sample Preparation

The epitaxially strained $Sr_{1-x}Ba_xTiO_3$ films where x = 0, 0.125, and 0.37 were grown on (110) $DyScO_3$, (110) $TbScO_3$, and (110) $GdScO_3$ single crystalline substrates via pulsed laser deposition (PLD) and using sintered ceramic targets with stoichiometric $SrTiO_3$, $Sr_{0.875}Ba_{0.125}TiO_3$, and $Sr_{0.63}Ba_{0.37}TiO_3$, respectively. The laser power was 5 J/cm^2 with a repetition rate of 1 Hz, the process gas was oxygen at a pressure of 1 Pa, and the growth temperature was 700℃. In order to obtain relatively homogeneously strained epitaxial films with reasonably large capacitive contributions, a layer thickness of 40 nm was chosen for all samples.

To analyse the film's in-plane dielectric properties, interdigitated electrodes (IDEs) were prepared on top of the $(Sr,Ba)TiO_3$ layer using e-beam lithography and a lift-off technique. The IDEs comprised a 5 nm-thick Cr adhesion layer and a 15 nm-thick Pt layer. The interdigitated structure consisted of 64 "fingers," each with an effective length of 700 μm,

resulting in an effective capacitor length of w = 63 × 700 µm = 44.1 mm (see Figure 6a). To simplify the data analysis, a relatively large gap of 5 µm was chosen. This geometry allows for the use of the partial capacitive model [35] to interpret the capacitive measurements.

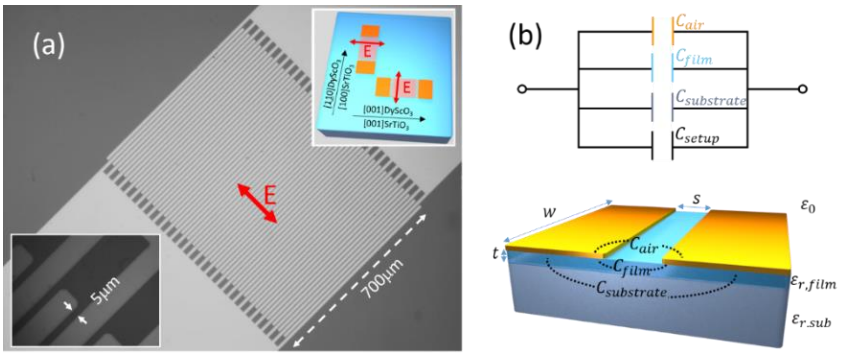

Figure 6. (a) Scanning electron microscopy image of the capacitor's IDE design and schematic view of the IDE design orientation with respect to the crystallographic directions of the substrate and film; (b) schematic view of the electric field distribution from the side view and the equivalent electric circuit.

According to the partial capacitance model, the total capacitance can be ascribed to four capacitive contributions (see Figure 6b):

$$C_{total} = C_{air} + C_{film} + C_{substrate} + C_{setup} \tag{2}$$

where C_{air}, C_{film}, $C_{substrate}$, and C_{setup} are the contributions of the ambient space (air), film, substrate, and experimental setup (e.g., cables and LCR meter), respectively. However, by performing a reference measurement of an identical system without the ferroelectric film, we obtain a reference capacitance $C_{reference} = C_{air} + C_{substrate} + C_{setup}$. The capacitance of the film is thus given by:

$$C_{film} = C_{total} - C_{reference} \tag{3}$$

The resulting permittivity can be obtained by conformal mapping according to [35]:

$$C_{film} = \{w \cdot \varepsilon_0(\varepsilon_{r,film} - \varepsilon_{r.sub})\}/\{s/t + 4ln2/\pi\} \quad (4)$$

where w is the effective length of the planar capacitor (obtained from the number and length of the IDE fingers), s the gap size of the capacitor, t the thickness of the film, ε_o the permittivity of free space, and ε_r the dielectric constant of the film and substrate, respectively (see Figure 6).

The surface of the (110) $DyScO_3$, (110) $TbScO_3$, and (110) $GdScO_3$ substrates exhibit a nearly square lattice with only a minor difference between the [1$\underline{1}$0] and [001] directions, referred to as the "short" and "long" axis in the following. Since the orthorhombic crystal structure of the rare-earth scandate substrates (lattice parameters a_o, b_o, c_o) can be approximated by a pseudocubic structure (lattice parameters a_p, b_p, c_p), the resulting pseudocubic in-plane lattice parameters are $a_p = \sqrt{a_o^2 + b_o^2}/2$ along [1$\underline{1}$0] direction and $b_p = c_o/2$ along [001] direction (see Figure 7).

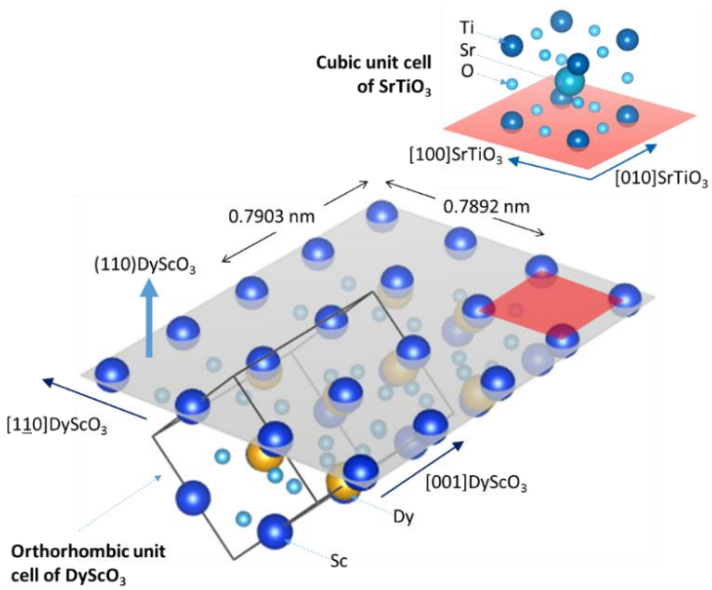

Figure 7. Schematic view of the epitaxial growth of $SrTiO_3$ on the rare-earth scandate $DyScO_3$.

Table 1. Lattice parameters of scandate *substrates used in this chapter*

Substrate	a_o (Å)	b_o (Å)	c_o (Å)	a_p (Å), [1$\underline{1}$0] direction	b_p (Å), [001] direction
$DyScO_3$ [36]	5.440	5.717	7.903	3.946	3.952
$TbScO_3$ [36]	5.466	5.731	7.917	3.960	3.959
$GdScO_3$ [36]	5.480	5.746	7.932	3.970	3.966

As a consequence, the epitaxial films experience a different in-plane strain for the two different directions. For the (110) $DyScO_3$ substrates, the [001] direction represents the "long" axis, whereas the [1$\underline{1}$0] direction is the "long" axis for the (110) $TbScO_3$ and (110) $GdScO_3$ substrates (see Table 1). The nominally cubic $SrTiO_3$ (and also the (Sr,Ba)TiO_3) adjusts the in-plane rectangular lattice structure of the different substrates. The in-plane primitive translation vectors [100] and [010] of $Sr_{1-x}Ba_xTiO_3$ are elongated and oriented along the [1$\underline{1}$0] and [001] directions of the substrate, whereas the [001] lattice parameter of (Sr,Ba)TiO_3 is oriented normal to the substrate surface [23]. To analyse the ferroelectric properties of the films in both major crystallographic directions, all samples are equipped with at least two IDE structures: one with the electric field $\vec{E}$ aligned along the short axis, the other with $\vec{E}$ aligned along the long axis.

3.2. Structural Characterization

Prior to cryoelectronic characterization, the crystalline structure and epitaxy of the (Sr,Ba)TiO_3 films is analysed via X-ray reciprocal space mapping (RSM). For the sake of clarity, the samples are arranged according to the strain and labelled *A* (smallest strain) to *E* (largest strain).

Figure 8 demonstrates the epitaxial quality of the strained (Sr,Ba)TiO_3 films. RSM data are shown for the two in-plane orientations of the substrates: the upper and lower figures reveal the lattice correlation in the [001] and [1$\underline{1}$0] substrate direction, respectively. Since the $q_{\parallel}$-values are identical for the film and the substrate (see dashed lines in Figure 8), the in-plane lattice parameters of the films correspond to those of the respective

substrates, i.e., it demonstrates the perfect epitaxy of the films. As a consequence, the difference between the lattice parameters of the strained and unstrained (stars in Figure 8) (Sr,Ba)TiO_3 increases from sample *A* (small strain) to sample *E* (large strain): $\Delta q_{\parallel} = q_{\parallel}(film) - q_{\parallel}(substrate)$ increases from sample *A* to sample *E*, whereas $\Delta q_{\perp} = q_{\perp}(film) - q_{\perp}(substrate)$ decreases from sample *A* to sample *E*. The film thus experiences more and more strain with increasing lattice mismatch between the film and the substrate. The tensile in-plane strain is partially compensated by a compressive out-of-plane strain. Using the RSM data in Figure 8, the lattice parameters and thus the nominal misfit strain of the films can be evaluated. Table 2 provides a summary of the lattice parameters and the resulting nominal misfit strain.

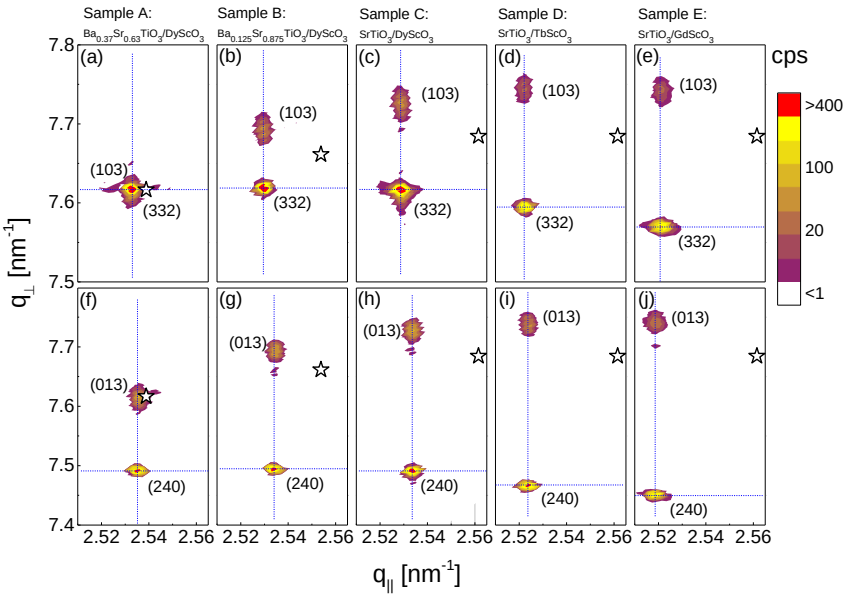

Figure 8. RSM of the XRD in the vicinity of the (332) (a-e) and the (240) (f-j) Bragg reflections of the substrates for samples A-E. The dashed lines and stars depict the positions of the strained film and the corresponding position for unstrained $Sr_{1-x}Ba_xTiO_3$ for various stoichiometries, respectively. Data adopted from Ref. [24].

Table 2. Lattice parameters (accuracy: ±0.001 Å) and resulting nominal strain of our strained $Sr_{1-x}Ba_xTiO_3$ films. The lattice parameters a_{ref} represent the literature value of unstrained material. In addition, Poisson-corrected values of the strain using a Poisson ratio of $\nu = 0.23$ (literature value for unstrained (Sr,Ba)TiO_3) are given in parentheses. This correction is discussed in section 3.3

	Film	Substrate	Lattice parameters of the films (Å)				Resulting strain (%)		
			Reference	Experimental values			ϵ_a	ϵ_b	ϵ_c
			a_{ref}	a	b	c			
A	$Sr_{0.63}Ba_{0.37}TiO_3$	$DyScO_3$	3.939	3.951	3.945	3.939	0.305 (0.219)	0.152 (0.067)	0.000 (-0.085)
B	$Sr_{0.875}Ba_{0.125}TiO_3$	$DyScO_3$	3.916	3.949	3.940	3.901	0.843 (0.810)	0.613 (0.580)	-0.383 (-0.415)
C	$SrTiO_3$	$DyScO_3$	3.904	3.951	3.946	3.882	1.204 (1.130)	1.076 (1.002)	-0.564 (-0.637)
D	$SrTiO_3$	$TbScO_3$	3.904	3.964	3.962	3.877	1.537 (1.403)	1.486 (1.352)	-0.692 (-0.823)
E	$SrTiO_3$	$GdScO_3$	3.904	3.971	3.966	3.875	1.716 (1.561)	1.588 (1.433)	-0.743 (-0.894)

To learn more about the strain-induced structural changes, we consider the in-plane areal lattice misfit and the volumetric change of the unit cell of the strained films. In a first approach, all misfit values are obtained by comparing the measured lattice parameters and the corresponding literature values for unstrained material (see Table 2). These values thus represent nominal values for the c-axis lattice misfit, in-plane areal misfit, and volume mismatch. In section 3.3, we show that these values must be corrected due to structural relaxation effects caused by defects in the material.

For small concentrations *x*, unstrained $Sr_{1-x}Ba_xTiO_3$ has a cubic lattice. Its lattice parameter exhibits a linear dependence on the change of the barium content at room temperature, which can be approximated by $a_{ref} = 3.904 + 0.094x$ (Å) for $x < 0.6$ [37, 38]. Using this reference value, we obtain a nominal lattice mismatch $\varepsilon_i = (i - a_{ref})/a_{ref}$ for each lattice parameter $i = a, b, c$. The values of the nominal lattice mismatch are summarized in Table 1. The resulting in-plane area mismatch is $(ab - a_{ref}^2)/a_{ref}^2$ and the volume mismatch is given by $(abc - a_{ref}^3)/a_{ref}^3$. The *c*-axis mismatch and the volume change are plotted as a function of the areal misfit in Figure 9. It shows a linear decrease of the *c*-axis (out-of-plane) lattice parameter of the films with increasing areal mismatch, thus indicating that the tensile in-plane strain is compensated by a shrinkage of the *c*-axis. However, it is only partially compensated, since the volume of the unit cell increases with increasing areal mismatch, as indicated by the solid data points in Figure 9. It is worth noting the linear dependence between the volumetric change and the in-plane strain, which not only reveals that the Poisson's ratio ν is identical for all films, but that the value of the Poisson ratio can also be derived for the strained films. This value transpires to be $\nu \approx 0.33$, which is larger than – but still close to – the literature value $\nu \approx 0.23$ reported for unstrained crystalline $SrTiO_3$ [39]. The increase of the Poisson ratio might be caused by defects in the films, which is addressed in the next section.

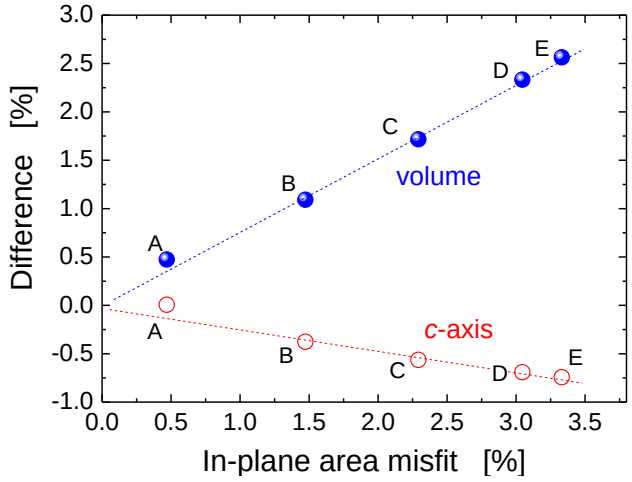

Figure 9. Changes of the unit cell volume (solid symbols) and c-axis (open symbols) as a function of the in-plane areal mismatch for samples A-E. The data are evaluated from the XRD data shown in Figure 8; the dashed lines indicate the linear dependence for both parameters. Data adopted from Ref. [24].

3.3. Engineering T_c via Epitaxial Strain

One of the best indicators for the modification of the ferroelectric properties is given by analysing the Curie temperature T_C. This is, for example, shown in Figure 1b for the impact of the stoichiometry of T_C. In the following, we discuss the impact that strain has on the Curie temperature. All other ferroelectric properties also appear to be altered accordingly. The best and most simple way of determining T_C is by analysing the Curie–Weiss fit $1/\varepsilon_r \cong (T - T_C)/C$ (Eq. (1)), as illustrated in Figure 4.

Figure 10 shows typical data obtained for the temperature-dependent permittivity of various epitaxially strained $SrTiO_3$ films. The Curie–Weiss fit provides the T_C values for a series of (Sr,Ba)TiO_3 films on different rare-earth scandate substrates [24]. By measuring the in-plane permittivity along the two major orientations ([001] and [1$\underline{1}$0] substrate directions), two T_C values are obtained for each sample. These values show a near-linear increase with the strain for each stoichiometry (see Figure 10b).

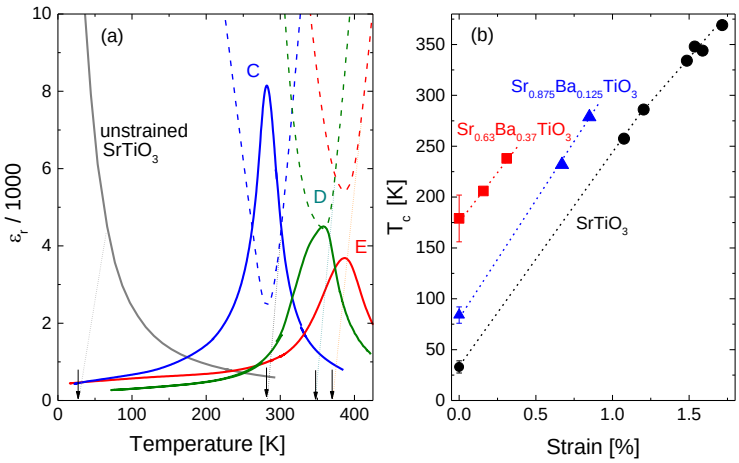

Figure 10. (a) Examples of the temperature dependence of the dielectric permittivity and (b) resulting strain dependence of the Curie–Weiss temperature for unstrained (Sr,Ba)TiO_3 and epitaxially strained (Sr,Ba)TiO_3 films. The dashed and dotted lines in (a) show the temperature dependence of the inverse permittivity and the Curie–Weiss fit (linear extrapolations), respectively. The arrows depict the resulting Curie–Weiss temperatures.

In order to analyse these data further, we (i) add reference values for zero strain, (ii) discuss the theoretical expectation of the strain dependence of T_C in terms of the Landau thermodynamic model, and consider the impact of (iii) the critical thickness and (iv) the resulting generation of defects on the shift of T_C.

3.3.1. Zero Strain Reference

In addition to the T_C values of the epitaxially strained films, we consider the reference value for unstrained (Sr,Ba)TiO_3. For small amounts of Ba, these values can be approximated by a simple polynomial of the 2nd order ($T_C = 36 + 356x$) [40-42] or 3rd order ($T_C = 30 + 484x + 136x^2$) [43-45], where T_C is given in units of K and x represents the stoichiometric value of the composition $(Sr_{1-x}Ba_x)TiO_3$. For small values of x, the resulting T_C values are fairly similar for both approaches. They are added as reference values for zero strain in Figure 10b.

3.3.2. Landau Theory

In general, the Landau theory represents a thermodynamic description of continuous phase transitions. As such, it can be used to predict T_C enhancement due to strain [18]. According to the Landau theory, the shift of the Curie–Weiss temperature due to an in-plane strain ϵ is given by:

$$\Delta T_C = T_{C.film} - T_{C.ref} = 2\varepsilon_0 C \frac{Q_{11}+Q_{12}}{s_{11}+s_{12}} \epsilon \tag{5}$$

where $T_{C.film}$ and $T_{C.ref}$ are the Curie temperatures of the strained film and of the corresponding unstrained materials, respectively; ε_0 is the permittivity of vacuum; C is the Curie–Weiss constant; and Q_{ij} and s_{ij} represent the electrostrictive coefficients and elastic compliances. The expected strain-induced change of T_C can be evaluated by inserting literature values for the parameters Q_{ij}, s_{ij}, and C (see Table 3).

Figure 11 summarizes all data, the experimental values of ΔT_C for the epitaxially strained (Sr,Ba)TiO_3 films and the theoretical predictions of the Landau theory (Eq. (5)) for $SrTiO_3$ and $BaTiO_3$. Up to $\epsilon \approx 1.2\%$, there is a near-perfect agreement between the experimental data and the theoretical prediction. Above $\epsilon \approx 1.2\%$, experimental data start to deviate from the expected linear strain dependence. One possible explanation might be the structural relaxation of the films due to defect formation in the films [24], as outlined in Figure 11.

Table 3. Parameters used for the thermodynamic prediction of ΔT_C according to the Landau theory (Eq. (5)) for $SrTiO_3$ and $BaTiO_3$

	$Q_{11} + Q_{12}$ (m^4/C^2)	$s_{11} + s_{12}$ (m^2/N)	C (K)	$T_{C.ref}$ (K)
$SrTiO_3$	-0.033 [46]	2.38×10^{-12} [47]	9×10^4 [44]	36
$BaTiO_3$	-0.065 [48]	5.65×10^{-12} [46]	12×10^4 [44]	393

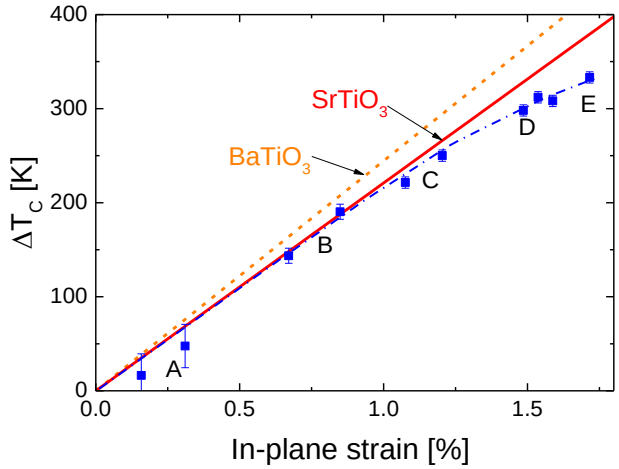

Figure 11. Enhancement of T_C as a function of the nominal in-plane strain for samples A to E (squares), and theoretical predictions according to Landau theory (Eq. (5)) for $SrTiO_3$ and $BaTiO_3$,(solid lines). Data adopted from Ref. [24].

3.3.3. Strain Relaxation Due to Defects

Misfit dislocations are one of the main contributors to strain relaxation. They are automatically generated during epitaxial film growth on lattice-mismatched substrates. These dislocations reduce the elastic energy and strain in the film [20, 49]. Equilibrium thermodynamic theories [50, 51] predict a *critical thickness* h_c, below which the film grows without defects or misfit dislocations, and above which defects are generated. The critical thickness can be approximated by [52]:

$$h_c = \left[\frac{b}{4\pi(1+\nu)\epsilon_0}\right]\left[\ln\left(\frac{h_c}{b}\right)+1\right] \quad (6)$$

where $\epsilon_0 = (a_{film} - a_{substrate})/a_{film}$ represents the nominal lattice misfit defined by the lattice parameters of the unstrained film (a_{film}) and the substrate ($a_{substrate}$) at growth conditions, b is the extension of the dislocation line, and ν is the Poisson's ratio. Assuming reasonable values of b = 0.4 nm and a Poisson's ratio of ν = 0.23 for unstrained (Sr,Ba)TiO_3 [39] or, alternatively, our experimental value of ν = 0.33 for strained (Sr,Ba)TiO_3

and literature values for the lattice parameters and thermal expansion coefficients of the film and substrates [36], the critical thickness of $(Sr,Ba)TiO_3$ can be estimated as a function of the lattice misfit. Figure 12 shows the expected critical thickness for the $(Sr,Ba)TiO_3$ system. Using in-plane lattice parameters for the substrates, the critical thickness can be estimated for samples A-E.

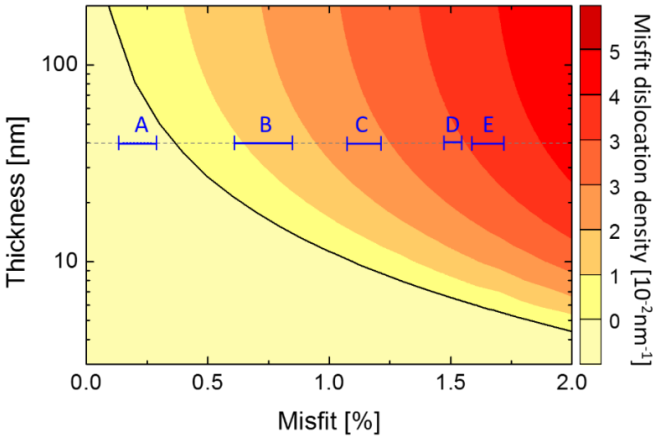

Figure 12. Critical thickness (solid line, left scale) for the generation of misfit dislocations according to Eq. (6) and misfit dislocation density (tone-filled contour plot, right scale) as a function of film thickness for the large strain direction according to Eq. (7). The data points denote the situation for the two major in-plane lattice directions of the 40 nm-thick A-E samples.

Epitaxial films generally grow fully strained until they reach critical thickness. Once the film reaches critical thickness, defects develop and the strain in the following layers decreases. As a result, the total effective strain of a film is smaller than the nominal strain once critical thickness is exceeded. Strain relaxation is therefore larger for films with smaller critical thicknesses, i.e., films with larger lattice mismatches.

The accumulation of misfit dislocations starts at the critical thickness and eventually leads to the complete relaxation of the strain if the films are sufficiently thick. Based on the equilibrium thermodynamic theory, the density of misfit dislocations is zero for $h < h_c$ and [53]:

$$\rho \cong \frac{\epsilon_0}{|\mathbf{b}| \cos\lambda}\left(1 - \frac{h_c}{h}\right), \text{for } h > h_c \quad (7)$$

where $|\mathbf{b}| \cos\lambda$ is the projection of the Burgers vector of the defect to the substrate surface. Assuming the most common slip system [101]<10$\underline{1}$> in perovskites [53], the Burgers vector is equivalent to the lattice parameter of $SrTiO_3$ at growth conditions [54]. The resulting equilibrium linear misfit dislocation density for our system is shown in Figure 12. Strain-induced dislocation defects appear in the film exceeding its critical thickness, which suggests that defects should not be expected for small strain (ϵ < 0.37% for the 40 nm-thick films), whereas for large strain, defects contribute significantly to a plastic relaxation of the strain. However, depending on the deposition process, there are usually more defects, such as oxygen vacancy (see section 5), in oxide films. Another quantitative way of estimating the impact of strain on the lattice parameter is based on Poisson's ratio. This is outlined in the following.

3.3.4. Effective Lattice Parameter

Based on the stress–strain relation, which in the simplest case is described by the Poisson's ratio v, an effective lattice parameter of the strained film [39]:

$$a_{eff} = \frac{va + vb + (1-v)c}{1+v} \quad (8)$$

where a, b are the in-plane lattice parameters and c is the out-of-plane lattice parameter. Inserting the Poisson's ratio (e.g., v = 0.23) and the experimentally determined lattice parameters (see Table 2), we obtain the effective intrinsic lattice parameter. The effective lattice parameters appear to be slightly larger than the nominal lattice parameters [55]. Moreover, with increasing lattice mismatch between the film and the substrate, and with film thicknesses larger than the critical thickness, a_{eff} increases and the tensile strain is thus increasingly overestimated. As a result, the value for the strain should be corrected using the effective lattice parameters.

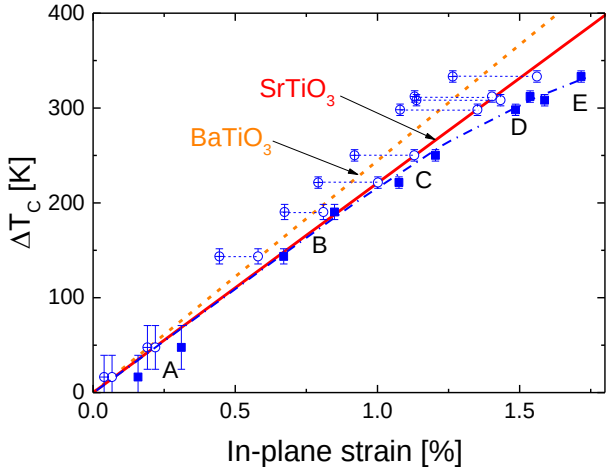

Figure 13. ΔT_C as a function of in-plane strain for samples A-E, corrected for strain relaxation and according to Eq. (8). The solid symbols represent the uncorrected data of Figure 11, whereas the open symbols represent the corrected values using a Poisson's ratio of ν = 0.23 (open circles) and ν = 0.33 (open circles with cross), respectively. The lines represent the theoretical predictions according to Landau theory Eq. (5)) for $SrTiO_3$ and $BaTiO_3$. Data adopted from Ref. [24].

The resulting corrected strain values are given in Table 2 and used in Figure 13. The figure shows an even better agreement between the theory and experiment, especially for a Poisson's ratio of 0.23.

Overall, the Curie temperature increases linearly with strain in $SrTiO_3$, even with small amounts of Sr being substituted with Ba. The scaling with ~(222 ± 20) K per 1% strain is in good agreement with the theoretical prediction of the thermodynamic Landau theory. The already good agreement between experiment and theory is further improved if corrections due to the defect-mediated strain relaxation are taken into account. The scaling of the Curie temperature with strain (Figure 13) can be used as a formula for engineering T_C and respective ferroelectric properties for many applications.

4. RELAXOR-TYPE BEHAVIOUR

The previous section showed how tensile strain can shift the transition temperature of epitaxial $SrTiO_3$ films towards, or even beyond, room temperature depending on the amount of strain. However, soon after the first observation of this effect in 2004 [18], it was noticed that these strain-modified ferroelectric films exhibit an unusual behaviour. In 2006, Biegalski et al. [56] suspected that strained $SrTiO_3$ films are relaxor ferroelectric. In 2010, Jang et al. [31] demonstrated relaxor behaviour in strain-free, non-stoichiometric $SrTiO_3$ films. They concluded that "strained and strain-free films, as well as single crystals of $SrTiO_3$ are relaxor ferroelectrics to varying degrees." A few years later, Lee et al. [34] demonstrated that strained $SrTiO_3$ films should not exhibit relaxor behaviour so long as the films are nominally stoichiometric and the defect concentration is sufficiently low.

At present, it can be concluded that the relaxor-type behaviour of $SrTiO_3$ films is not due to the strain but rather the concentration of defects. However, as demonstrated in the previous section, epitaxially strained $SrTiO_3$ films tend to possess a large density of defects and are therefore prone to be relaxor-type ferroelectrics. This is one of the reasons why relaxor ferroelectrics are discussed in this chapter. Another reason is that relaxor ferroelectricity itself is an interesting effect, which possesses a number of interesting properties.

4.1. What Is Relaxor-Type Ferroelectricity?

Although relaxor ferroelectrics (or relaxors) were discovered in the $BaTiO_3$-$BaSnO_3$ system in 1954 [57], the mechanism for this effect is yet to be fully understood [58]. The field of relaxor research has experienced a revival of interest in recent years, largely thanks to research on strained ferroelectrics. Compositional disorder, i.e., the disorder in the arrangement of different ions on crystallographically equivalent sites, is the common feature of relaxors. As such, relaxors represent a class of *disordered ferroelectric crystals* with particular properties (see Figure 14) that are

correlated to the formation of polar nanoregions (PNR). At high temperatures, relaxors exist in a non-polar paraelectric phase, which is similar to the paraelectric phase of ordinary ferroelectrics. Upon cooling, they transform into an ergodic relaxor state, in which polar regions are formed on the nm scale with a random orientation of dipole moment. This transformation occurs at Burns temperature T_B, which is defined as the temperature at which permittivity deviates from the Curie–Weiss behaviour. In principle, this transition is not considered a structural phase transition since it is not accompanied by any change of crystal structure on the macroscopic or mesoscopic scale. Nevertheless, the polar nanoregions have a significant impact on the ferroelectric properties of the crystalline material. For this reason, the state of the crystalline material at $T < T_B$ is often considered to be a new phase, the *relaxor ferroelectric phase*.

At temperatures close to T_B, the PNRs are mobile and behave ergodically. Upon cooling, their mobility slows down and at freezing temperature T_F, the PNRs freeze in a nonergodic state, again without any structural phase transition. This nonergodic relaxor state is similar to a dipole glass or spin glass phase. It can irreversibly transform into the ordinary ferroelectric state either in a spontaneous manner or with the help of a sufficiently strong electric field. A number of possible scenarios for transitions of states in relaxors are illustrated in Ref. [58]; the scenario observed in strained $SrTiO_3$ is shown in Figure 14.

The freezing of the PNR dynamics is associated with a broad peak in the temperature dependence of the permittivity with a characteristic frequency dispersion (see Figure 14). The peak of the permittivity at T_{max} is of the same order of magnitude as the peak at the Curie temperature T_c in ordinary ferroelectrics. However, it is highly diffuse and its temperature T_{max} decreases with frequency. The pattern of the temperature dependence of the permittivity and the shift of T_{max} with frequency are both characteristics of relaxor behaviour. They are discussed in the next section for the case of strained $SrTiO_3$.

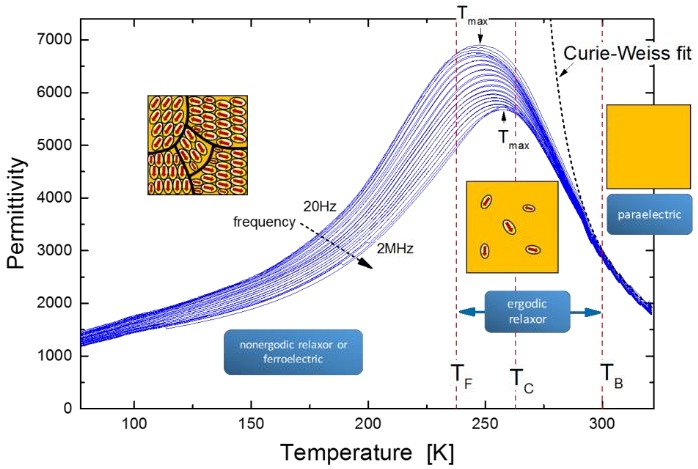

Figure 14. Permittivity as a function of temperature and frequencies ranging from 20 Hz (largest permittivity) to 2 MHz (smallest permittivity) for a thin epitaxially strained $SrTiO_3$ film on (110) $DyScO_3$ with the electric field parallel to the [1$\underline{1}$0] $DyScO_3$ direction. The data are adopted from Ref. [23]. Characteristic temperatures (Vogel–Fulcher freezing temperature T_F, Curie temperature T_C, temperature of maximum permittivity T_{max}, and Burns temperature T_B) are indicated; the Curie–Weiss fit of the paraelectric state is given; and schematic illustrations of the evolution of PNRs are shown.

4.2. Relaxor Behaviour in Epitaxially Strained $SrTiO_3$ Films

Figure 14 shows the typical relaxor behaviour of an epitaxially strained $SrTiO_3$ film, which is most likely caused by the defects induced by the strain (see section 3.3). It reveals the characteristic broad peak in the temperature dependence of the permittivity and the shift of this peak with frequency.

The ferroelectric phase transition should generally scale in the temperature regime $T > T_{max}$ according to the empirical Lorentz-type relation [59]:

$$\frac{\varepsilon_{r,max}}{\varepsilon_r} - 1 = \frac{(T-T_{max})^{\gamma}}{2\sigma} \tag{9}$$

where $\varepsilon_{r,max} = \varepsilon_r(T_{max})$, σ, and γ represent the maximum in the permittivity at T_{max}, the degree of diffuseness of the phase transition, and the

degree of dielectric relaxation, respectively. For an ordinary ferroelectric, a sharp phase transition where $\gamma = 1$ is expected. The diffusion of the phase transition leads to an increase of γ. Larger values of γ thus indicate the tendency towards a relaxor-type behaviour, while values of $\gamma = 2$ are considered to be characteristic for relaxor ferroelectrics [59, 60]. The Lorentz-type scaling of the transition is typically demonstrated in a log–log plot of the normalized permittivity $(\varepsilon_{r,max} - \varepsilon_r)/\varepsilon_r$ versus $(T-T_{max})$. Figure 15a shows this plot for the data of the epitaxially strained $SrTiO_3$ film on (110) $DyScO_3$, as seen in Figure 14. The log–log plot reveals the expected linearity with a slope of $\gamma \approx 2$ demonstrating the relaxor-type behaviour of this strained $SrTiO_3$ film.

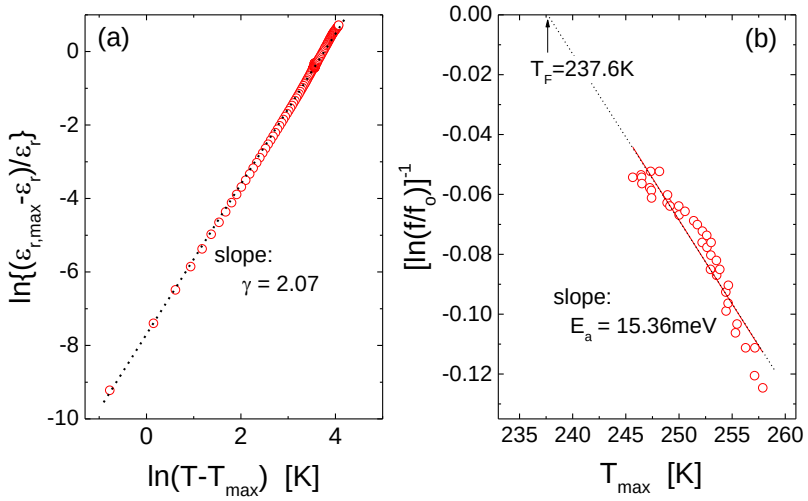

Figure 15. (a) Lorentz fit (Eq. (9)) and (b) Vogel–Fulcher fit (Eq. (10) with an attempt frequency of 4 GHz) of the permittivity at 1 MHz for the epitaxially strained $SrTiO_3$ film shown in Figure 14. The linear behaviour of the fits yields data of (a) $\gamma = 2.07$ and (b) $T_F \approx 237.6$ K and $E_a \approx 15.4$ meV.

The second typical feature of relaxor ferroelectrics is given by the frequency dispersion, which is most prominent at the transition to the relaxor ferroelectric state. Figure 14 shows the temperature dependence of the

permittivity for different frequencies (20 Hz to 2 MHz). Especially for the peak at T_{max} – i.e., close to the transition – large differences are recorded with respect to the permittivity for different frequencies. With decreasing frequency, permittivity increases while T_{max} decreases. This frequency dispersion is described by the Vogel–Fulcher equation [61, 62]:

$$f = (2\pi\tau_o)^{-1} exp\left[\frac{E_a}{k_B(T_{max}-T_F)}\right] \quad (10)$$

with the attempt frequency $f_o = (2\pi\tau_o)^{-1}$ typically of the order of the phonon frequencies 1-10 GHz, the activation energy E_a, Boltzmann constant k_B, and the static freezing temperature T_F. The resulting *Vogel–Fulcher fit* of the permittivity data shown in Figure 14 is given in Figure 15b. It shows the expected linear relation between the reduced frequency $[ln(f/f_o)]^{-1}$ and T_{max}. Inserting a reasonable value for the attempt frequency f_o yields values for the static freezing temperature T_F and activation energy E_a. For instance, for f_o = 4 GHz, we obtain values of $T_F \approx 237.6$ K and $E_a \approx 15.4$ meV for the strained $SrTiO_3$ film. The evaluated E_a value represents a typical value for the activation energy of relaxor ferroelectrics [31, 63].

Therefore, unless extreme care is taken to avoid defects, the tensile epitaxial strain not only leads to an enhancement of the transition temperature but also a relaxor-type behaviour in $SrTiO_3$ films.

4.3. High Tunability of Strained $SrTiO_3$

The permittivity of the relaxor-type ferroelectric $SrTiO_3$ films not only depends on frequency, it can also be tuned by an applied electric field. Since both mechanisms are based on the limited mobility of the PNRs, they share certain similarities. The electric tunability of the epitaxially strained $SrTiO_3$ films can be extremely high and reveals a number of interesting relaxor properties. An interesting example of a DC-bias-dependent measurement of the permittivity is given in Figure 16 [23].

The experiment shows different steps and mechanisms for the electric tuning of these relaxor ferroelectric films:

1. Tunability is initially extremely high. At T_C, for example, permittivity is drastically reduced to only ~11% of the original value (i.e., measured before exposure to a DC electric field) with a DC bias of 8 V/μm.

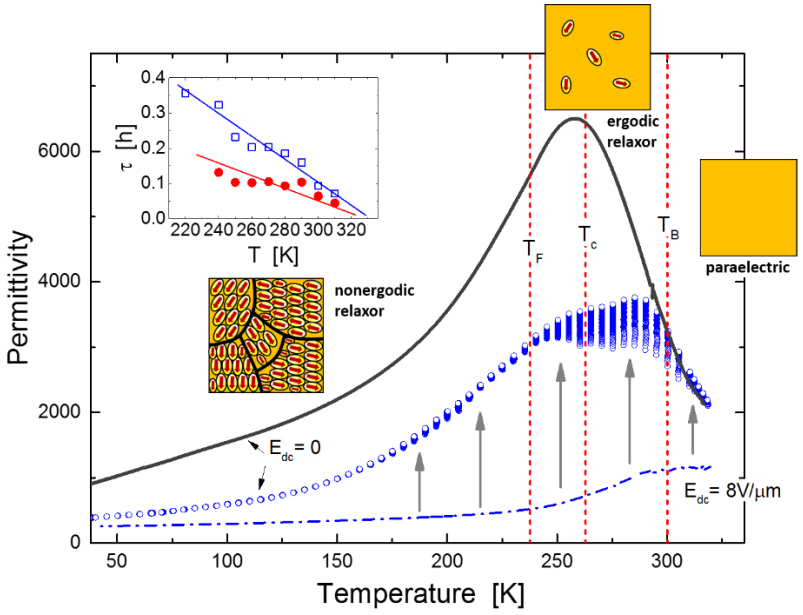

Figure 16. Example of the high DC bias tunability and its relaxation for the strained relaxor-type $SrTiO_3$ film (sample identical to that of Figures 14 and 15), depicting the original (i.e., initial zero-bias) permittivity (solid line), the subsequent permittivity obtained if a DC electric field of 8V/μm is applied parallel to [1$\underline{1}$0] $DyScO_3$ (dashed-dotted line), and the upward relaxation of the permittivity over time, which is obtained after removing the DC electrical field (open circles). The inset shows the relaxation times τ_1 and τ_2 obtained from the exponential fit for short-term relaxation (t < 9 min, solid symbols) and long-term relaxation (t > 9 min, open symbols), respectively. Data adopted from Ref. [23].

2. After releasing the electric field, the permittivity of the relaxor does not return to its original value but remains at significantly lower

values. For T_C, permittivity only returns to ~47% of the original value.

3. Furthermore, there is a significant further relaxation of the permittivity after the release of the electric field. This relaxation is particularly pronounced for the ergodic temperature regime. For the example T_C, permittivity relaxes within approximately ½ hour from ~47% to 56% of the original value.

The initial high tunability and its only partial reversibility are associated with the (partially) irreversible transformation of the ergodic or nonergodic relaxor state into an ordinary ferroelectric state. This is characteristic for relaxor ferroelectrics that are suddenly exposed to a sufficiently strong electric field.

A further significant relaxation of permittivity is present in the ergodic state above freezing temperature. In this temperature regime, the PNRs become mobile again. The process demonstrates the typical exponential relaxation behaviour according to $\varepsilon_r \propto exp(-t/\tau)$ with a characteristic relaxation time constant of $\tau = 1/R$ and a relaxation rate R. For more complex systems, the distribution of relaxation rates or stretched exponential functions [64] are required to describe the relaxation process. In our investigation, the relaxation can be described by two relaxation constants, τ_1 and τ_2, which characterize the short-term relaxation and long-term relaxation, respectively. The inset of Figure 16 shows both relaxation time constants:

1. The relaxation times are very long at low temperatures and decrease linearly with temperature. At room temperature, relaxation rates of $R_1 = 1/\tau_1 \approx 5$ mHz and $R_2 = 1/\tau_2 \approx 2.7$ mHz are obtained. Relaxation times in the order of hour(s) (i.e., relaxation rates below 1 mHz) are not uncommon for relaxor ferroelectrics [65]. They indicate a large distribution in the mobility of the PNRs with randomly distributed directions of dipole moments [58, 66]. The large distribution itself is an indication of the large distribution in size and orientation of the micro- or even nano-sized domains in the strained $SrTiO_3$ film.

2. τ_1 and τ_2 tend towards zero, slightly above the Burns temperature. This is consistent with the observation that PNRs survive up to temperatures slightly above T_B [23].

Finally, Figure 17 shows very promising examples of different bias applications at smaller electric fields, that (i) are more reasonable for applications and (ii) do not lead to an irreversible transition to the ferroelectric state. In this example, DC and AC bias are applied. In both cases, a very large impact of the electric field remains visible. Interestingly, whereas the DC bias leads to a reduction of permittivity, the AC bias increases permittivity. Therefore, the combination of DC and AC bias opens up a wide range of tunability in these materials.

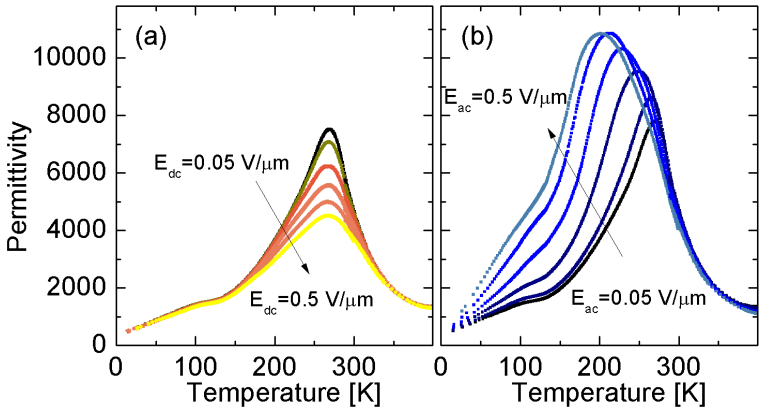

Figure 17. Example of the DC and AC tunability of an epitaxially strained $SrTiO_3$ film ($SrTiO_3$ on (110) $DyScO_3$ with electric field parallel to [001] $DyScO_3$, depicting (a) the DC tunability recorded with an AC field of 50 mV/μm and (b) the AC tunability. In both cases, the fields increase in the direction of the arrow from 0.05, 0.1, 0.2, 0.3, and 0.4, to 0.5 V/μm.

5. Strain-Engineered Conductivity of $SrTiO_3$

The conductivity of semiconductors and isolators is based on the excitation of electrons into the conduction band and the generation of holes in the valence band. Since both processes are thermally activated processes, conductivity increases with temperature for these materials (see Figure 18). The band gap separating the valence and conduction bands depends on the type of material: for the semiconductor materials seen in Figure 18, it is typically >1 eV, for isolators it should be >2.5 eV. As a result, the typical conductivity at room temperature is in the range of (10^{-6}-10^{2}) S/m for semiconductors and $<10^{-6}$ S/m for insulators. This conductivity can be modified by various means, for example by varying stoichiometry, doping, defects, and strain.

Stoichiometric, undoped, and unstrained $SrTiO_3$ is a d^0 band insulator with an indirect band gap energy of 3.25 eV and a direct band gap energy of 3.75 eV [67]. Similar to many other transition metal oxides, the valence band of $SrTiO_3$ mainly corresponds to the contributions of the O *2p* states, while the conduction band mainly originates from the Ti *3d* states. Consistent with the ionic structure of this material, the excited oxygen *2p* states in the valence band correspond to the formation of O^{2-} ions, whereas the empty Ti *3d* states (holes) in the conduction band represent the nominal Ti^{4+} valence state.

Due to the large band gap, $SrTiO_3$ crystals are typically transparent, whereas non-stoichiometric crystals lose their transparency and turn a dark blue, even blackish, colour. This modification is usually induced by extrinsic *dopants* and/or *oxygen vacancies*. Possible dopants range from trivalent ions such as Al^{3+}, La^{3+} ions on Sr^{2+} sites or pentavalent ions such as Nb^{5+}, Ta^{5+} ions on Ti^{4+} sites as donors, and Fe^{3+} as trivalent ions on Ti^{4+} sites, or Na^{+} as a monovalent dopant on Sr^{2+} as acceptors. Perhaps even more important are the defects based on non-stoichiometry, which are automatically induced if the preparation parameters are varied [68]. Due to their mobility, oxygen vacancies play a particularly important role in the resulting modification of the conductivity. As is discussed later, strain boosts the formation of oxygen vacancies, their mobility in $SrTiO_3$, and thus the conductivity of this material (see Figure 19).

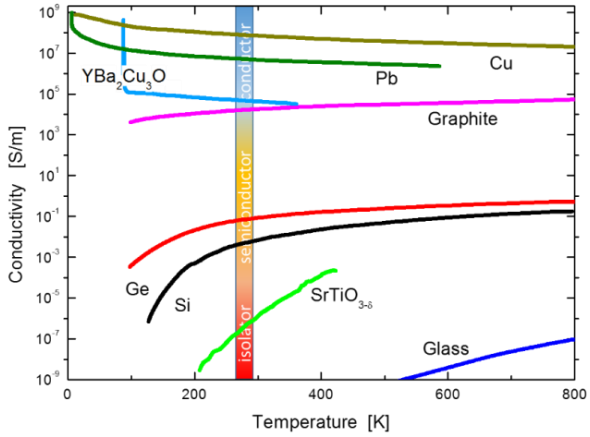

Figure 18. Conductivity of typical conductors (Cu, Pb, $YBa_2Cu_3O_7$, and graphite), semiconductors (Ge and Si), and isolators (glass and $SrTiO_{3-\delta}$ [13]) as a function of temperature.

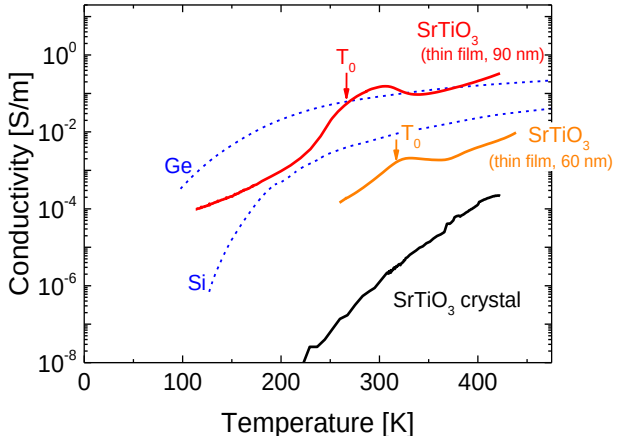

Figure 19. Comparison of the temperature-dependent conductivity of conventional semiconductors (Si, Ge), unstrained $SrTiO_3$ single crystals, and epitaxially strained $SrTiO_3$ films on (110) $DyScO_3$ substrates of different thicknesses. The ferroelectric phase transition temperature T_o of the strained $SrTiO_3$ films is indicated in the figure.

The formation of an *oxygen vacancy* (reduction) is described in Kröger–Vink notation by:

$$O_O^x \leftrightharpoons V_{\ddot{O}} + 2e' + \frac{1}{2}O_2(g) \quad (11)$$

where O_O^x represents the incorporated O^{2-} anion, $O_2(g)$ the oxygen molecule in the gas phase, $V_{\ddot{O}}$ the oxygen vacancy, and e' the free electron. The oxygen ion leaves the crystal and forms a neutral gas molecule. During this process, it releases two electrons and leaves behind a double positively charged oxygen vacancy.

5.1. Transport Properties of Strained $SrTiO_3$ films

Epitaxial strain is also used to modify the density and mobility of oxygen vacancies and thus the electric transport properties of strained $SrTiO_3$ films:

1. Lattice distortions modify the *band structure* of $SrTiO_3$ [68] and affect the occupation of the oxygen *2p* orbitals. This contributes to the density of states at the Fermi level and enhances conductivity in the direction of tensile strain [69].
2. Defects (most likely *oxygen vacancies*) are automatically generated to compensate for the strain in the film [24, 70]. Moreover, the mobility of oxygen vacancies is enhanced by the strain [71]. Whilst both effects are expected to lead to enhanced conductivity, in the case of tensily strained $SrTiO_3$, the latter effect favours the electronic plasticity of these films, which is important for neuromorphic devices, for example.
3. Since a structural transition the phase transition T_o, the mobility of the defects (oxygen vacancies) is expected to be enhanced at T_o [72, 73]. The shift of T_o via strain (see section 3) presents a third option for modifying the conductivity of $SrTiO_3$ via strain.

All these features (with the exception of the electronic plasticity, which is discussed in section 5.2) can be seen in Figure 19, which compares the conductivity of conventional semiconductors (Si, Ge), unstrained $SrTiO_3$ single crystals, and two epitaxially strained $SrTiO_3$ films on (110) $DyScO_3$

substrates of different thicknesses. The conductivity of $SrTiO_3$ at room temperature is enhanced from the isolator regime for the defect-free single crystal with $\sigma_{300K} \approx 10^{-6}$ S/m to the semiconducting regime for the strained films. In the case of $SrTiO_3$ on (110) $DyScO_3$, the conductivity σ_{300K} ranges between ~10^{-4} S/m and ~1 S/m depending on the density, distribution, and mobility of defects (most likely oxygen vacancies) due to strain. Moreover, at the phase transition (shown in Figure 19), we observe a peak in conductivity. This peak supports the expected enhancement of oxygen mobility at the phase transition, while also representing an ideal operation regime for electronic devices such as memristors and e-synapses (see section 5.2).

5.1.1. Impact of the Metal–$SrTiO_3$ Interface

Since oxide electronic devices typically include metallic contacts, their impact on the oxide must be taken into account. The choice of metal is known to significantly affect electronic transport at the metal–oxide interface [74, 75]. For instance, Ti electrodes on TiO_2 create a high density of oxygen vacancies at the Ti–TiO_2 interface [76], which affects the resistive behaviour of oxide films [77-79]. Similar effects are expected for the metal–$SrTiO_3$ interface.

A comparison of the current–voltage characteristic of strained $SrTiO_3$ equipped with metal electrodes fabricated from Ti or the noble metal Pt reveals a clearly visible difference (see Figure 20). The Ti electrodes lead to a much larger conductivity of the $SrTiO_3$ film compared to the sample with Pt electrodes. Similar to observations for Ti–TiO_2 interfaces [72], this is most likely caused by the high density of oxygen vacancies generated at the Ti–$SrTiO_3$ interface [76, 80]. This higher vacancy density not only leads to larger conductivity, it also results in different conduction mechanisms. Whereas the large vacancy density at the Ti–$SrTiO_3$ interface results in an ohmic behaviour at low electric fields, Schottky-type behaviour according to $\ln J \propto \sqrt{E}$ is observed for the Pt–$SrTiO_3$ interface [81]. Moreover, the greater mobility of oxygen vacancies observed for strained $SrTiO_3$ compared to unstrained materials (see next section) enhances the impact of oxygen vacancies on the conductivity in these materials. We ultimately observe a

~30 times larger conductivity of ~70 A/cm^2 at 1 V/μm and at room temperature for the strained $SrTiO_3$ with Ti electrodes compared to its counterpart equipped with Pt electrodes (see Figure 20).

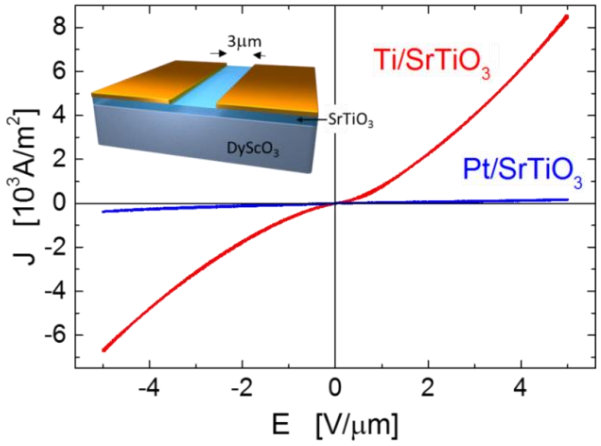

Figure 20. Current–voltage characteristic at room temperature for a 90 nm-thick strained $SrTiO_3$ film measured with Ti and Pt electrodes (gap size: 3 μm), respectively.

5.1.2. Device Design Issues

Another particular way of tailoring the conductivity (and especially the electronic plasticity) of $SrTiO_3$ is through the design of the device. Special electrode designs can be chosen to generate large electric field gradients, which lead to currents that are sufficient for the local heating of the film. Both electric field and the thermal effect in combination with oxygen vacancy mobility determine the oxygen vacancy drift and can be used to modify the performance of the device. This process is known as *electroformation*.

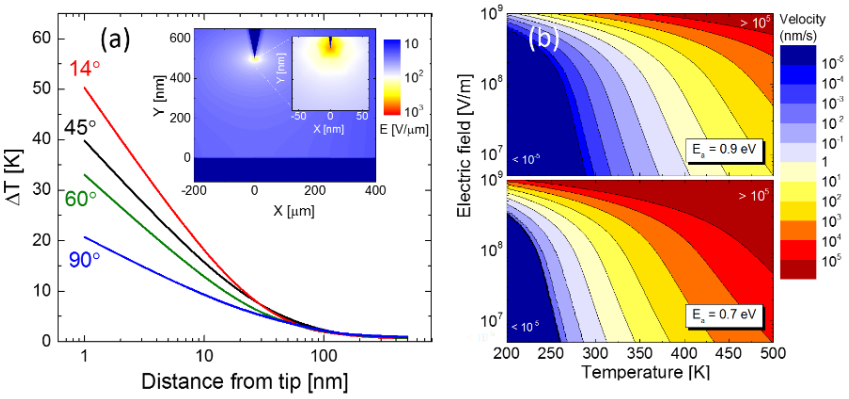

Figure 21. (a) Simulation of initial 2D electric field distribution for a 14° tapered electrode opposing a flat electrode at a distance of 500 nm on $SrTiO_3$, assuming an applied voltage of 30 V (inset) and the resulting change of temperature as a function of the distance from the tip in the direction of the flat electrode for different angles of the tapered electrode on strained $SrTiO_3$ film. (b) Expected field and temperature dependence of the drift velocity of oxygen vacancies according to Eq. (14) using activation energies of 0.9 eV and 0.7 eV for unstrained and tensile-strained $SrTiO_3$, respectively.

A typical electrode design is the combination of a sharp-tipped electrode opposing a flat electrode (see Figure 21). The expected 2D electric field distribution can be evaluated, for example, via the finite-difference time-domain method, using typical parameters for the conductivity of strained $SrTiO_3$ thin films [13]. The field gradient is generally largest at the tip of the tapered electrode and increases with the sharpness of the tip (see Figure 21). This electric field gradient leads to a current flow and, therefore, to a local heating of the film.

The resulting temperature distribution in the $SrTiO_3$ film is determined by electronic heating of the $SrTiO_3$ between the electrodes and cooling provided by the substrate. All other thermal effects can be disregarded. The thermal energy induced by a current in a small volume V is:

$$Q_{in} = I^2Rt = cm\Delta T \tag{12}$$

where I is the current flowing through volume V; R and m are the resistance and mass of V; c is the specific heat of $SrTiO_3$; t is the duration of the current

pulse; and ΔT is the resulting change in temperature. The heat flow through an area a^2 at the interface between the film and the substrate is:

$$Q_{out} = ka^2 \frac{T_{surface} - T_{substrate}}{h} t \tag{13}$$

where k is the thermal conductivity and h the thickness of the film. Inserting reasonable values for our $SrTiO_3$ films, for example c = 30 cal/mol·K [82] and k = 6 W/(m·K) [83], it is possible to evaluate the time τ after which the temperature in the $SrTiO_3$ film is stable (here, other effects such as plasticity, i.e., the migration of oxygen vacancies, are not considered). Assuming $Q_{in} = Q_{out}$ in the stable state, we obtain a value of $\tau \leq 5$ µs for our $SrTiO_3$ films with a thickness of $h < 100$ nm. After only a few microseconds, a stable temperature distribution is thus obtained during electroformation or pulse experiments in our $SrTiO_3$ film.

With these equations and the assumption that the substrate represents a large heat sink at a constant temperature (i.e., room temperature), the temperature distribution in the initial microseconds of a current pulse can be estimated. Figure 21 shows the change of temperature in the in-plane direction pointing from the tip of the tapered electrode to the flat electrode. The temperature increase generally peaks at the tip and reduces significantly with the distance to the tip. Moreover, ΔT increases with the increasing sharpness of the tip.

The drift velocity of the oxygen vacancies can be described by the Mott–Gurney equation [79]:

$$v = df exp\left(-\frac{E_A}{kT}\right) \sinh\left(\frac{zd}{2kT} E\right) \tag{14}$$

where d represents the hopping distance; f is the attempt frequency; E_A is the activation energy; z is the charge of the ion; and E is the electric field. Inserting reasonable values – for example d = 4 Å for $SrTiO_3$, z = 2 for double positively charged oxygen vacancies, an attempt frequency of $f = 6.67 \times 10^{12}$ Hz [79], and an activation energy for oxygen vacancies of 0.9 eV and 0.7 eV for unstrained and tensile-strained $SrTiO_3$ [71],

respectively – it is possible to simulate the mobility of oxygen vacancies in unstrained and strained $SrTiO_3$ as a function of electric field and temperature.

The resulting comparison of the drift velocities for strained and unstrained $SrTiO_3$ (see Figure 21b) reveals a number of interesting features. Firstly, oxygen vacancy mobility is generally higher in strained $SrTiO_3$ than in unstrained $SrTiO_3$. From the simulation of the electric field, the electric field regime can be estimated for a given design and applied voltage. For the case illustrated in Figure 21a, the electric field between the two electrodes ranges between $\sim 10^7$ and $\sim 2 \times 10^8$ V/m. In this case, the mobility of oxygen vacancies is in the order of 1 nm/s to 10 nm/s for strained $SrTiO_3$, which is 100 times larger than for unstrained $SrTiO_3$. Secondly, mobility is further enhanced by the local heating of the $SrTiO_3$. As shown in Figure 21a, the local temperature can be easily enhanced by several tens of K at the sharp tip. Due to this temperature increase, the velocity of oxygen vacancy migration is further enhanced at the position of the highest field gradient.

These considerations reveal that the combination of strained $SrTiO_3$ and an optimized electrode design (e.g., sharp tip and a flat electrode) lead to a high mobility of the oxygen vacancies. Moreover, it can be used to obtain an electronic plasticity similar to the plasticity observed in neuronal systems. This forms the basis for *neuromorphic devices*, which is discussed in the following.

5.2. E-synapse Made from Strained $SrTiO_3$

Motivated by the brain, which is capable of remembering, learning, and processing information in an energy-efficient and fault-tolerant manner, the development of *neuromorphic* systems –electronic systems that can mimic the function of the brain – is currently generating significant interest [84, 85]. In contrast to the classical von Neumann architecture, the neuromorphic architecture is able to tackle a number of issues, such as the processor-memory bottleneck and the rigid design problems, due to its intimate processor-memory combination and its “learning” capability. Similar to the

synapse in the brain (see Figure 22a), an artificial synapse is one of the most basic elements in the neuromorphic system. It represents a special type of two-terminal memristor, namely an *electronic synapse* (e-synapse), which, in addition to its ultra-low power consumption, possesses two important properties: the classical switching and a new feature, plasticity. The latter allows the e-synapse to be modified by switching, i.e., its ability to "learn" and "forget."

There are a number of electronic systems that exhibit synapse-like behaviour. They can be classified according to their mechanism into interface-barrier-based, filament-based, and other (e.g., spin or phase change) e-synapses. For instance, molecular and ionic thin-film memristive systems are based on the mobility of defects in the materials [86, 87], insulator-to-metal phase transition-driven memristors use the phase transition caused by Joule heating [88], and ferroelectric memristors utilize the electronically driven polarization of the materials [89, 90]. One of the most pursued types of memristor is based on uniform versus non-uniform oxygen diffusion in oxides [72]. In this type of material, oxygen vacancies play the most significant role in resistive switching behaviour. Various explanations have been given for the diffusion of oxygen vacancies, ranging from the development of conductive filaments [91], the modulation of the interface barrier height [76], and space-charge-limited current effects [92]. Controlling oxygen vacancy diffusion in such materials is one of the major issues faced by these promising types of memristor, especially in the case of a "learning" e-synapse.

Generally, perovskite materials and especially $SrTiO_3$ are ideal candidates for the active element of an e-synapse, since their conductivity can be easily modified by simply changing their defect concentration. This can be achieved, for instance, by Cr doping [93], a variation of the temperature or oxygen partial pressure during film growth [94], or thermal treatment at elevated temperatures [95]. Since the mobility of oxygen vacancies is still quite low after such modification, a vertical electrode–oxide–electrode arrangement consisting of sandwich structures with extremely thin films is used in most cases (see Figure 22b). In contrast, the combination of strain and design can lead to a larger mobility of oxygen

vacancies in $SrTiO_3$. This allows for larger structures and more flexibility in the design of e-synapses. For example, planar e-synapse structures or extended multi-electrode designs are a possibility (see Figure 22c) [13]. Moreover, the small peak in conductivity at the phase transition (see Figure 19) might even lead to a more stable working regime [13]. Using adequate strain, this peak can be shifted to room temperature [18], a temperature at which e-synapses should typically be operated.

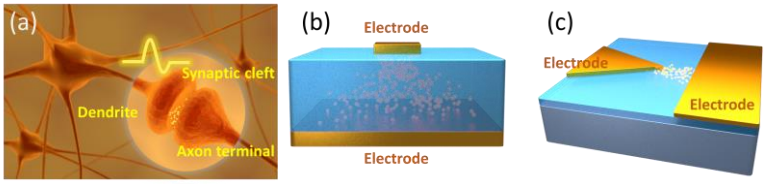

Figure 22. Schematics of (a) a biological synapse and two versions of memristor-type oxide e-synapses in a (b) vertical and (c) planar configuration.

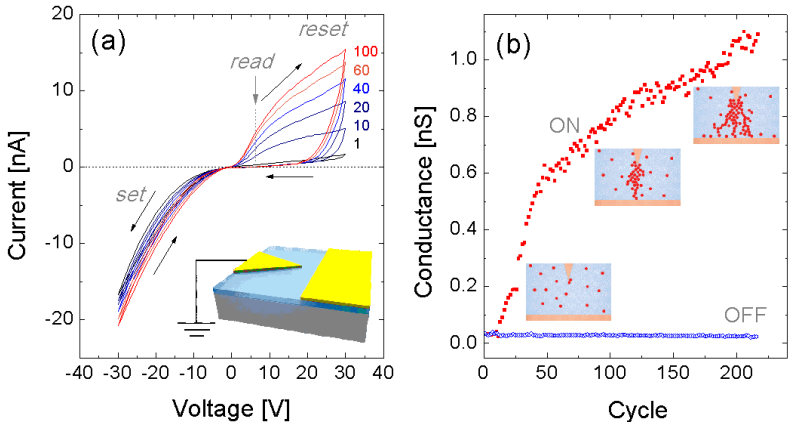

Figure 23. IVCs of an e-synapse consisting of an asymmetric pair of Ti electrodes (a flat electrode and a tapered (14˚) electrode at a distance of 500 nm (schematic view in (a)) on a 90 nm-thick strained $SrTiO_3$ film on $DyScO_3$. (a) Series of subsequently recorded IVCs demonstrating e-synaptic behaviour. The numbers indicate the number of cycles; the positions for set, reset, and read are indicated. (b) Time dependence of the read signal recorded at a read voltage of 5 V for the ON state (solid squares) and OFF state (open circles).

Figure 23 shows results obtained for an e-synapse on strained $SrTiO_3$. The asymmetric Ti electrode design consists of a sharp tip opposing a flat electrode (see schematic view in the figure). The distance between both electrodes is 500 nm; the sharpness of the tip is 14°. Figure 23a depicts the memristor behaviour as well as the plasticity, which are both essential characteristics of an e-synapse. In this measurement, a continuous voltage sweep is applied to the electrodes; the values shown adjacent to the curves indicate the number of the successive voltage cycle (not all cycles are shown). The current–voltage characteristics (IVCs) demonstrate the typical memristor behaviour with a high conductance in the ON state and a low conductance in the OFF state. However, while the OFF state remains low, the ON state increases with an increasing number of cycles (shown for a read voltage of 5 V in Figure 23b). This plasticity (in analogy to the synaptic behaviour of biological systems) is known from the literature [96]. It represents a gradual process defined by the migration of oxygen vacancies (see schematic views in Figure 23b). The vacancies initially form very thin channels that only allow for a small transport current. With each loop, the channels grow wider until the local electrical field gradient becomes too weak to support any further migration of oxygen vacancies.

For negative voltages ("set voltage", electrons move from the flat electrode towards the tip), a Poole–Frenkel (PF) behaviour [97, 98], in which electrons are trapped in localized states, is observed [13]. Due to thermal fluctuation, the electrons can be spontaneously excited to the conduction band and move (hop) under the impact of an electric field to another trapping side. The voltage barrier which the electrons must overcome to hop between the defects in the strained $SrTiO_3$ is approximately ϕ_B = 0.28 eV. With an increasing number of cycles, more percolative defect channels are formed between both electrodes, which automatically impact the effective density of defects between the electrodes.

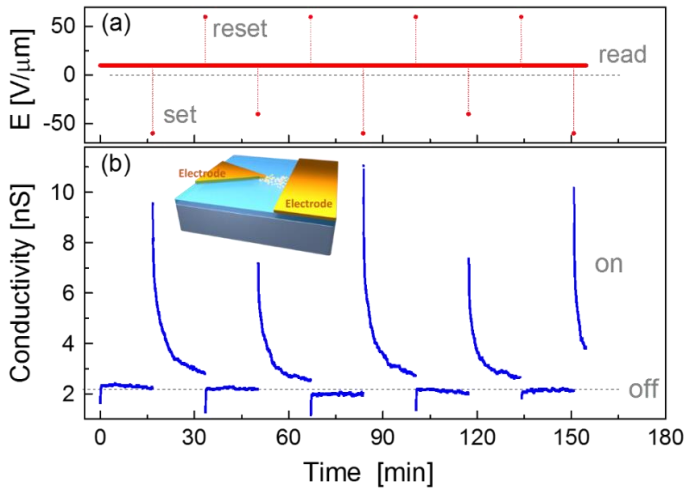

Figure 24. Plasticity of a planar e-synapse based on a strained $SrTiO_3$ film on $DyScO_3$, obtained via (a) a train of voltage pulses with resets (+60 V/µm for 5 s), 2 types of sets (-60 V/µm and -20 V/µm for 5 s), and continuous reading at 10 V/µm. (b) shows the resulting read conductivity in the OFF state (after reset) and the plasticity (in this case "forgetting") of the ON state for both types of set. Note that larger set voltages lead to larger initial read signals in the ON state; the exponential decay of the signal is identical in both cases. Data adopted from Ref. [13].

For positive voltages ("read" and "reset"), electrons move from the tip to the flat electrode. Firstly, a large conductivity marks the ON state of the e-synapse. However, at sufficiently high voltages, oxygen vacancies are pushed away from the flat electrode, which causes a disruption of the conductive defect channels ("reset"). These gaps significantly reduce the conductance of the e-synapse, resulting in the low-conducting OFF state. In the OFF state, the IVCs exhibit no plasticity. Moreover, they exhibit the expected space-charge-limited current [99] with the characteristic $I \propto V^{1/2}$.

Finally, the plasticity of the e-synapse can be demonstrated for these devices via different series of pulse measurements, varying repetition rate, frequency, pulsed duration, and amplitude. These measurements are aimed at demonstrating the ability of these devices to "learn" and "forget," similar to the synaptic long-term and short-term potentiation/depression or spike-time-dependent plasticity. A typical example of such an experiment is shown

in Figure 24. Similar to the biological synapse, two different mechanisms can be identified that cause plasticity in a planar e-synapse based on strained $SrTiO_3$ [13]:

1. A fast process defined by the ionic dipole formation (polarization) in the strained $SrTiO_3$ with a typical mean relaxation time of $\tau \cong$ 100 ps.
2. A slow process defined by the mobility of oxygen vacancies with a typical mean relaxation time of $\tau \cong 10$ s at room temperature. The latter process is dependent on the amplitude, duration, repetition rate of the set and reset pulses, and on the initial state of the synapse.

In summary, the electronic transport properties of $SrTiO_3$ thin films can be engineered via epitaxial strain. The resulting films can be used as active components in applications ranging from conventional memristors to novel neuromorphic devices (e.g., e-synapses).

SUMMARY AND CONCLUSION

In this chapter, we demonstrated that the extraordinary electric properties of the transition metal oxide $SrTiO_3$ can be utilized through adequate tuning of the material. In contrast to conventional methods, which are typically based on doping, mixing, or adding other oxides to this material, we outlined how the properties of epitaxial $SrTiO_3$ films can be improved via mechanical strain. We reported in detail on:

- *Engineering the ferroelectric transition*: Using epitaxially strained $(Sr,Ba)TiO_3$ films on various rare-earth scandate substrates, we demonstrated a near-linear increase of the Curie temperature with the nominal strain caused by the lattice mismatch between the film and the substrate. Taking small corrections into account due to plastic strain relaxation caused by strain-induced defect formation in the film, we obtained a perfect linear strain dependence of the

Curie temperature, which is in perfect agreement with the Landau thermodynamic theory predicting an increase of the Curie temperature with ~(222±20) K per 1% strain. This temperature scaling can be used as a case study for the engineering of T_C and correlated ferroelectric properties for many applications.

- *Relaxor-type behaviour:* Considering the huge impact of the strain on T_C, it appears to be possible to move T_C as well as the ferroelectric transition to room temperature. This shift of T_C not only affects the ferroelectric properties at room temperature, leading, for example, to high-k materials with room temperature permittivities of several thousand, it also affects the type of ferroelectricity in these materials. The epitaxially strained films typically exhibit textbook-like relaxor-type behaviour with a broad ferroelectric transition and freezing temperatures slightly below the Curie temperature. In the ergodic state, and also for small electric fields in the nonergodic state, an extremely high tunability of the permittivity with DC and AC fields is observed.
- *Tuning the conductivity*: Even the conductance of the nominally isolating material can be modified by epitaxial strain. With adequate strain, $SrTiO_3$ not only becomes semiconductor-like, it also exhibits electronic plasticity. Both properties make this system ideal for applications ranging from memristor to neuromorphic devices, such as artificial synapses (e-synapses). The flexibility of planar e-synapse designs might lead to complex neuromorphic computing processes being performed, for example, with short-term and long-term memory using planar nanoscale electrode arrays.

In general, epitaxially strained $SrTiO_3$ films represent an ideal system for understanding the role and mechanism of elastic strain in engineering the ferroelectric and electric properties of metal oxides. On the one hand, this knowledge can support the utilization of $SrTiO_3$ in various applications ranging from high-k components, highly tunable varactors, and memristors to neuromorphic devices. On the other hand, it has catalysed ongoing research into similar systems. It has led, for example, to research on the

impact of compressive strain on the metal oxide $NaNbO_3$ with a ferroelectric transition temperature significantly above room temperature [100-102]. The transition temperature was shown to be reduced in a similar way using compressive strain instead of tensile strain. In this way, it has been used to optimize the piezoelectric metal oxide $(K,Na)NbO_3$, making it suitable for applications such as surface acoustic wave-based sensors or actuators [103, 104]. Other systems will most likely follow. This all serves to indicate a highly promising future for strain engineering of functional oxides.

REFERENCES

[1] Wilk, G. D., Wallace, R. M., Anthony, J. 2001. "High-κ Gate Dielectrics: Current Status and Materials Properties Considerations." *J. Appl. Phys.* 89:5243-5275.

[2] Lemanov, V., Smirnova, E., Syrnikov, P., Tarakanov, E. 1996. "Phase Transitions and Glasslike Behavior in $Sr_{1-x}Ba_xTiO_3$." *Phys. Rev. B* 54:3151-3157.

[3] Scott, J. 2007. "Applications of Modern Ferroelectrics." *Science* 315:954-959.

[4] Waser, R., Dittmann, R., Staikov, G., Szot, K. 2009. "Redox-Based Resistive Switching Memories - Nanoionic Mechanisms, Prospects, and Challenges." *Adv. Mater.* 21:2632-2663.

[5] Ribes, G., Mitard, J., Denais, M., Bruyere, S., Monsieur, F., Parthasarathy, C., Vincent, E., Ghibaudo, G. 2005. "Review on High-k Dielectrics Reliability Issues." *IEEE Trans. Device Mater. Reliab.* 5:5-19.

[6] Petzelt, J., Ostapchuk, T., Gregora, I., Rychetsky, I., Hoffmann-Eifert, S., Pronin, A. V., Yuzyuk, Y., Gorshunov, B. P., Kamba, S., Bovtun, V., Pokorny, J., Savinov, M., Porokhonskyy, V., Rafaja, D., Vanek, P., Almeida, A., Chaves, M. R., Volkov, A. A., Dressel, M., Waser, R. 2001. "Dielectric, Infrared, and Raman Response of Undoped $SrTiO_3$ Ceramics: Evidence of Polar Grain Boundaries." *Phys. Rev. B* 64:184111.

[7] Momma, K., Izumi, F. 2011. "VESTA 3 for Three-dimensional Visualization of Crystal, Volumetric and Morphology Data." *J. Appl. Crystallogr.* 44:1272-1276.

[8] Bancroft, D. 1938. "The Effect of Hydrostatic Pressure on the Susceptibility of Rochelle Salt." *Phys. Rev.* 53:587-590.

[9] Forsbergh Jr, P. 1954. "Effect of a Two-dimensional Pressure on the Curie Point of Barium Titanate." *Phys. Rev.* 93:686-692.

[10] Nguyen, L. D., Brown, A. S., Thompson, M. A., Jelloian, L. M. 1992. "50-nm Self-aligned-gate Pseudomorphic AlInAs/GaInAs High Electron Mobility Transistors." *IEEE Trans. Electron. Devices* 39:2007-2014.

[11] Yildiz, B. 2014. "“Stretching” the Energy Landscape of Oxides—Effects on Electrocatalysis and Diffusion." *MRS Bull.* 39:147-156.

[12] Bardeen, J., Shockley, W. 1950. "Deformation Potentials and Mobilities in Non-polar Crystals." *Phys. Rev.* 80:72-80.

[13] Dai, Y. 2017. "Tailoring the Electronic Properties of Epitaxial Oxide Films via Strain for SAW and Neuromorphic Applications." *Schriften des Forschungszentrums Jülich, Key Technologies, Volume 169, ISBN 978-3-95806-319-8.*

[14] Sato, H., Naito, M. 1997. "Increase in the Superconducting Transition Temperature by Anisotropic Strain Effect in (001) $La_{1.85}Sr_{0.15}CuO_4$ Thin Films on $LaSrAlO_4$ substrates." *Physica C* 274:221-226.

[15] Beach, R., Borchers, J., Matheny, A., Erwin, R., Salamon, M., Everitt, B., Pettit, K., Rhyne, J., Flynn, C. 1993. "Enhanced Curie Temperatures and Magnetoelastic Domains in Dy/Lu Superlattices and Films." *Phys. Rev. Lett.* 70:3502-3505.

[16] Gan, Q., Rao, R., Eom, C., Garrett, J., Lee, M. 1998. "Direct Measurement of Strain Effects on Magnetic and Electrical Properties of Epitaxial $SrRuO_3$ Thin Films." *Appl. Phys. Lett.* 72:978-980.

[17] Fuchs, D., Arac, E., Pinta, C., Schuppler, S., Schneider, R., Löhneysen, H. v. 2008. "Tuning the Magnetic Properties of $LaCoO_3$ Thin Films by Epitaxial Strain." *Phys. Rev. B* 77:014434.

[18] Haeni, J. H., Irvin, P., Chang, W., Uecker, R., Reiche, P., Li, Y. L., Choudhury, S., Tian, W., Hawley, M. E., Craigo, B., Tagantsev, A. K.,

Pan, X. Q., Streiffer, S. K., Chen, L. Q., Kirchoefer, S. W., Levy, J., Schlom, D. G. 2004. "Room-temperature Ferroelectricity in Strained $SrTiO_3$." *Nature* 430:758-761.

[19] Choi, K. J., Biegalski, M., Li, Y., Sharan, A., Schubert, J., Uecker, R., Reiche, P., Chen, Y., Pan, X., Gopalan, V. 2004. "Enhancement of Ferroelectricity in Strained $BaTiO_3$ Thin Films." *Science* 306:1005-1009.

[20] Hollmann, E., Schubert, J., Kutzner, R., Woerdenweber, R. 2009. "Stress Generated Modifications of Epitaxial Ferroelectric $SrTiO_3$ Films on Sapphire." *J. Appl. Phys.* 105:114104.

[21] Warusawithana, M. P., Cen, C., Sleasman, C. R., Woicik, J. C., Li, Y., Kourkoutis, L. F., Klug, J. A., Li, H., Ryan, P., Wang, L.-P. 2009. "A Ferroelectric Oxide Made Directly on Silicon." *Science* 324:367-370.

[22] Lee, J. H., Fang, L., Vlahos, E., Ke, X., Jung, Y. W., Kourkoutis, L. F., Kim, J. W., Ryan, P. J., Heeg, T., Roeckerath, M. 2010. "A Strong Ferroelectric Ferromagnet Created by Means of Spin–lattice Coupling." *Nature* 466:954-958.

[23] Wördenweber, R., Schubert, J., Ehlig, T., Hollmann, E. 2013. "Relaxor Ferro- and Paraelectricity in Anisotropically Strained $SrTiO_3$ Films." *J. Appl. Phys.* 113:164103.

[24] Dai, Y., Schubert, J., Hollmann, E., Mussler, G., Wördenweber, R. 2016. "Engineering of the Curie Temperature of Epitaxial $Sr_{1-x}Ba_xTiO_3$ Films via Strain." *J. Appl. Phys.* 120:114101.

[25] Cardona, M. 1965. "Optical Properties and Band Structure of $SrTiO_3$ and $BaTiO_3$." *Phys. Rev.* 140:A651-A655.

[26] Riess, I. 2003. "Mixed Ionic–electronic Conductors — Material Properties and Applications." *Solid State Ion.* 157:1-17.

[27] Vendik, O., Zubko, S. 2000. "Ferroelectric Phase Transition and Maximum Dielectric Permittivity of Displacement Type Ferroelectrics ($Ba_xSr_{1-x}TiO_3$)." *J. Appl. Phys.* 88:5343-5350.

[28] Sakayori, K.-i., Matsui, Y., Abe, H., Nakamura, E., Kenmoku, M., Hara, T., Ishikawa, D., Kokubu, A., Hirota, K.-i., Ikeda, T. 1995. "Curie Temperature of $BaTiO_3$." *Jpn. J. Appl. Phys.* 34:5443-5445.

[29] Pertsev, N., Zembilgotov, A., Tagantsev, A. 1998. "Effect of Mechanical Boundary Conditions on Phase Diagrams of Epitaxial Ferroelectric Thin Films." *Phys. Rev. Lett.* 80:1988-1991.

[30] Schlom, D. G., Chen, L.-Q., Eom, C.-B., Rabe, K. M., Streiffer, S. K., Triscone, J.-M. 2007. "Strain Tuning of Ferroelectric Thin Films." *Annu. Rev. Mater. Res.* 37:589-626.

[31] Jang, H., Kumar, A., Denev, S., Biegalski, M. D., Maksymovych, P., Bark, C., Nelson, C. T., Folkman, C., Baek, S. H., Balke, N. 2010. "Ferroelectricity in Strain-free $SrTiO_3$ Thin Films." *Phys. Rev. Lett.* 104:197601.

[32] Li, Y., Choudhury, S., Haeni, J., Biegalski, M., Vasudevarao, A., Sharan, A., Ma, H., Levy, J., Gopalan, V., Trolier-McKinstry, S. 2006. "Phase Transitions and Domain Structures in Strained Pseudocubic (100) $SrTiO_3$ Thin Films." *Phys. Rev. B* 73:184112.

[33] Biegalski, M. D., Vlahos, E., Sheng, G., Li, Y., Bernhagen, M., Reiche, P., Uecker, R., Streiffer, S., Chen, L., Gopalan, V. 2009. "Influence of Anisotropic Strain on the Dielectric and Ferroelectric Properties of $SrTiO_3$ Thin Films on $DyScO_3$ substrates." *Phys. Rev. B* 79:224117.

[34] Lee, C.-H., Skoromets, V., Biegalski, M. D., Lei, S., Haislmaier, R., Bernhagen, M., Uecker, R., Xi, X., Gopalan, V., Martí, X. 2013. "Effect of Stoichiometry on the Dielectric Properties and Soft Mode Behavior of Strained Epitaxial $SrTiO_3$ Thin Films on $DyScO_3$ Substrates." *Appl. Phys. Lett.* 102:082905.

[35] Vendik, O., Zubko, S., Nikol'Skii, M. 1999. "Modeling and Calculation of the Capacitance of a Planar Capacitor Containing a Ferroelectric Thin Film." *Techn. Phys.* 44:349-355.

[36] Uecker, R., Velickov, B., Klimm, D., Bertram, R., Bernhagen, M., Rabe, M., Albrecht, M., Fornari, R., Schlom, D. G. 2008. "Properties of Rare-earth Scandate Single Crystals (Re=Nd−Dy)." *J. Cryst. Growth* 310:2649-2658.

[37] Wong-Ng, W., Yang, Z., Kaduk, J. A., Cook, L. P., Diwanji, S., Lucas, C. 2011. "Interactions of $Ba_2YCu_3O_{6+x}$ with $SrTiO_3$ Substrate." *Physica C* 471:250-257.

[38] Liu, R. S., Cheng, Y. C., Chen, J. M., Liu, R. G., Wang, J. L., Tsai, J. C., Hsu, M. Y. 1998. "Crystal and Electronic Structures of (Ba, Sr)TiO_3." *Mater. Lett.* 37:285-289.

[39] Christen, H. M., Specht, E. D., Silliman, S. S., Harshavardhan, K. S. 2003. "Ferroelectric and Antiferroelectric Coupling in Superlattices of Paraelectric Perovskites at Room Temperature." *Phys. Rev. B* 68:020101.

[40] Dul'kin, E., Zhai, J., Roth, M. 2015. "Relaxor–ferroelectric Crossover Seen via Characteristic Temperatures of $Ba_xSr_{1-x}TiO_3$ Ferroelectrics Detected by Acoustic Emission." *Phys. Status Solidi (b)* 252:2079-2083.

[41] Rupprecht, G., Bell, R. 1962. "Microwave Losses in Strontium Titanate above the Phase Transition." *Phys. Rev.* 125:1915-1920.

[42] Jackson, W., Reddish, W. 1945. "High Permittivity Crystalline Aggregates." *Nature* 156:717-717.

[43] Tinte, S., Stachiotti, M., Phillpot, S., Sepliarsky, M., Wolf, D., Migoni, R. 2004. "Ferroelectric Properties of $Ba_xSr_{1-x}TiO_3$ Solid Solutions Obtained by Molecular Dynamics Simulation." *J. Phys.: Condens. Matter* 16:3495-3506.

[44] Hilton, A., Ricketts, B. 1996. "Dielectric Properties of Ceramics." *J. Phys. D: Appl. Phys.* 29:1321-1325.

[45] Hoffmann, S., Waser, R. 1998. "Curie-Weiss Law of $(Ba_{1-x}Sr_x)TiO_3$ Thin Films Prepared by Chemical Solution Deposition." *J. Phys. IV* 8:Pr9-221-Pr9-224.

[46] Kvasov, A., Tagantsev, A. K. 2012. "Positive Effective Q_{12} Electrostrictive Eoefficient in Perovskites." *J. Appl. Phys.* 112:094106.

[47] Kityk, A. V., Schranz, W., Sondergeld, P., Havlik, D., Salje, E. K. H., Scott, J. F. 2000. "Low-frequency Superelasticity and Nonlinear Elastic Behavior of $SrTiO_3$ Crystals." *Phys. Rev. B* 61:946-956.

[48] Wang, J. J., Meng, F. Y., Ma, X. Q., Xu, M. X., Chen, L. Q. 2010. "Lattice, Elastic, Polarization, and Electrostrictive Properties of $BaTiO_3$ from First-principles." *J. Appl. Phys.* 108:034107.

[49] Wördenweber, R., Grellmann, T., Greben, K., Schubert, J., Kutzner, R., Hollmann, E. 2012. "Stress Generated Modifications of Structural and Morphologic Properties of Epitaxial $SrTiO_3$ Films on Sapphire." *Ferroelectrics* 430:57-64.

[50] Van der Merwe, J. 1963. "Crystal Interfaces. Part I. Semi- Infinite Crystals." *J. Appl. Phys.* 34:117-122.

[51] Matthews, J., Blakeslee, A. 1974. "Defects in Epitaxial Multilayers: I. Misfit Dislocations." *J. Cryst. Growth* 27:118-125.

[52] Matthews, J., Jackson, D., Chambers, A. 1975. "Effect of Coherency Strain and Misfit Dislocations on the Mode of Growth of Thin Films." *Thin Solid Films* 26:129-134.

[53] Speck, J. S., Pompe, W. 1994. "Domain Configurations due to Multiple Misfit Relaxation Mechanisms in Epitaxial Ferroelectric Thin Films. I. Theory." *J. Appl. Phys.* 76:466-476.

[54] Ban, Z. G., Alpay, S. P. 2002. "Phase Diagrams and Dielectric Response of Epitaxial Barium Strontium Titanate Films: A Theoretical Analysis." *J. Appl. Phys.* 91:9288-9296.

[55] Yamanaka, T., Hirai, N., Komatsu, Y. 2002. "Structure Change of $Ca_{1-x}Sr_xTiO_3$ Perovskite with Composition and Pressure." *Am. Miner.* 87:1183-1189.

[56] Biegalski, M., Jia, Y., Schlom, D., Trolier-McKinstry, S., Streiffer, S., Sherman, V., Uecker, R., Reiche, P. 2006. "Relaxor Ferroelectricity in Strained Epitaxial $SrTiO_3$ Thin Films on $DyScO_3$ Substrates." *Appl. Phys. Lett.* 88:192907.

[57] Smolenskii, G. A., Isupov, V. A. 1954. "Ferroelectric Properties of Solid Solutions of Barium Stannate in Barium Titanate." *Zh. Tekhn. Fiz.* 24:1375-1386 [*Sov. J. Tech. Phys*. 24:1375-1386].

[58] Bokov, A., Ye, Z. G. 2006. "Recent Progress in Relaxor Ferroelectrics with Perovskite Structure." *J. Mater. Sci.* 41:31-52.

[59] Bokov, A., Ye, Z. G. 2000. "Phenomenological Description of Dielectric Permittivity Peak in Relaxor Ferroelectrics." *Solid State Comm.* 116:105-108.

[60] Bokov, A., Bing, Y. H., Chen, W., Ye, Z. G., Bogatina, S., Raevski, I., Raevskaya, S., Sahkar, E. 2003. "Empirical Scaling of the Dielectric Permittivity Peak in Relaxor Ferroelectrics." *Phys. Rev. B* 68:052102.

[61] Fulcher, G. S. 1925. "Analysis of Recent Measurements of the viscosity of Glasses." *J. Am. Ceram. Soc.* 8:339-355.

[62] Vogel, H. 1921. "The Temperature Dependence Law of the Viscosity of Fluids." *Phys. Z.* 22:645-646.

[63] Viehland, D., Jang, S., Cross, L. E., Wuttig, M. 1990. "Freezing of the Polarization Fluctuations in Lead Magnesium Niobate Relaxors." *J. Appl. Phys.* 68:2916-2921.

[64] Kohlrausch, R. 1854. "Theorie des Elektrischen Rückstandes in der Leidener Flasche." *Ann. Phys.-Berlin* 167:179-214.

[65] Gladkiĭ, V., Kirkov, V., Ivanova, E., Volk, T. 2006. "Anomalies of Polarization Processes in Relaxor Ferroelectrics." *Phys. Solid State* 48:1106-1110.

[66] Cross, L. E. 1987. "Relaxor Ferroelectrics." *Ferroelectrics* 76:241-267.

[67] van Benthem, K., Elsässer, C., French, R. H. 2001. "Bulk Electronic Structure of $SrTiO_3$: Experiment and Theory." *J. Appl. Phys.* 90:6156-6164.

[68] Hashimoto, S., Poulsen, F. W., Mogensen, M. 2007. "Conductivity of $SrTiO_3$ Based Oxides in the Reducing Atmosphere at High Temperature." *J. Alloys Compds.* 439:232-236.

[69] Wang, B., You, L., Ren, P., Yin, X., Peng, Y., Xia, B., Wang, L., Yu, X., Poh, S. M., Yang, P., Yuan, G., Chen, L., Rusydi, A., Wang, J. 2013. "Oxygen-driven Anisotropic Transport in Ultra-thin Manganite Films." *Nat. Commun.* 4:2778.

[70] Choi, S. Y., Kim, S. D., Choi, M., Lee, H. S., Ryu, J., Shibata, N., Mizoguchi, T., Tochigi, E., Yamamoto, T., Kang, S.-J. L. 2015. "Assessment of Strain-generated Oxygen Vacancies Using $SrTiO_3$ Bicrystals." *Nano Lett.* 15:4129-4134.

[71] Al-Hamadany, R., Goss, J. P., Briddon, P. R., Mojarad, S. A., O'Neill, A. G., Rayson, M. J. 2013. "Impact of Tensile Strain on the Oxygen

Vacancy Migration in $SrTiO_3$: Density Functional Theory Calculations." *J. Appl. Phys.* 113:224108.

[72] Bock, J. A., Lee, S., Trolier-McKinstry, S., Randall, C. A. 2015. "Metallic-like to Nonmetallic Transitions in a Variety of Heavily Oxygen Deficient Ferroelectrics." *Appl. Phys. Lett.* 107:092902.

[73] Tiwari, A., Jin, C., Narayan, J. 2002. "Strain-induced Tuning of Metal – Insulator Transition in $NdNiO_3$." *Appl. Phys. Lett.* 80:4039-4041.

[74] Mikheev, E., Hoskins, B. D., Strukov, D. B., Stemmer, S. 2014. "Resistive Switching and its Suppression in Pt/Nb:$SrTiO_3$ Junctions." *Nat. Commun.* 5:3990.

[75] Abe, K., Komatsu, S. 1992. "Epitaxial Growth of $SrTiO_3$ Films on Pt Electrodes and Their Electrical Properties." *Jpn. J. Appl. Phys.* 31:2985-2988.

[76] Yang, J. J., Pickett, M. D., Li, X., Ohlberg, D. A., Stewart, D. R., Williams, R. S. 2008. "Memristive Switching Mechanism for Metal / Oxide/Metal Nanodevices." *Nat. Nanotechnol.* 3:429-433.

[77] Shen, J., Lee, H., Valentí, R., Jeschke, H. O. 2012. "Ab initio Study of the Two-dimensional Metallic State at the Surface of $SrTiO_3$: Importance of Oxygen Vacancies." *Phys. Rev. B* 86:195119.

[78] Kubicek, M., Schmitt, R., Messerschmitt, F., Rupp, J. L. 2015. "Uncovering Two Competing Switching Mechanisms for Epitaxial and Ultrathin Strontium Titanate-based Resistive Switching Bits." *ACS Nano* 9:10737-10748.

[79] Starschich, S., Menzel, S., Böttger, U. 2016. "Evidence for Oxygen Vacancies Movement During Wake-up in Ferroelectric Hafnium Oxide." *Appl. Phys. Lett.* 108:032903.

[80] Joshua Yang, J., Miao, F., Pickett, M. D., Ohlberg, D. A., Stewart, D. R., Lau, C. N., Williams, R. S. 2009. "The Mechanism of Electroforming of Metal Oxide Memristive Switches." *Nanotechnology* 20:215201.

[81] Hwang, C. S., Lee, B. T., Kang, C. S., Lee, K. H., Cho, H. J., Hideki, H., Kim, W. D., Lee, S. I., Lee, M. Y. 1999. "Depletion Layer Thickness and Schottky Type Carrier Injection at the Interface

between Pt Electrodes and (Ba,Sr)TiO_3 Thin Films." *J. Appl. Phys.* 85:287-295.

[82] Hatta, I., Shiroishi, Y., Müller, K. A., Berlinger, W. 1977. "Critical Behavior of the Heat Capacity in $SrTiO_3$." *Phys. Rev. B* 16: 1138-1145.

[83] Breckenfeld, E., Wilson, R., Karthik, J., Damodaran, A. R., Cahill, D. G., Martin, L. W. 2012. "Effect of Growth Induced (Non)Stoichiometry on the Structure, Dielectric Response, and Thermal Conductivity of $SrTiO_3$ Thin Films." *Chem. Mater*. 24:331-337.

[84] Silver, D., Huang, A., Maddison, C. J., Guez, A., Sifre, L., Van Den Driessche, G., Schrittwieser, J., Antonoglou, I., Panneershelvam, V., Lanctot, M. 2016. "Mastering the Game of Go with Deep Neural Networks and Tree Search." *Nature* 529:484-489.

[85] Krogh, A. 2008. "What are Artificial Neural Networks?" *Nat. Biotechnol*. 26:195-197.

[86] Jo, S. H., Chang, T., Ebong, I., Bhadviya, B. B., Mazumder, P., Lu, W. 2010. "Nanoscale Memristor Device as Synapse in Neuromorphic Systems." *Nano Lett.* 10:1297-1301.

[87] Yang, Y., Gao, P., Gaba, S., Chang, T., Pan, X., Lu, W. 2012. "Observation of Conducting Filament Growth in Nanoscale Resistive Memories." *Nat. Commun.* 3:732.

[88] Driscoll, T., Kim, H. T., Chae, B. G., Di Ventra, M., Basov, D. 2009. "Phase-transition Driven Memristive System." *Appl. Phys. Lett.* 95:043503.

[89] Chanthbouala, A., Garcia, V., Cherifi, R. O., Bouzehouane, K., Fusil, S., Moya, X., Xavier, S., Yamada, H., Deranlot, C., Mathur, N. D., Bibes, M., Barthelemy, A., Grollier, J. 2012. "A Ferroelectric Memristor." *Nat. Mater*. 11:860-864.

[90] Kim, D. J., Lu, H., Ryu, S., Bark, C. W., Eom, C. B., Tsymbal, E. Y., Gruverman, A. 2012. "Ferroelectric Tunnel Memristor." *Nano Lett.* 12:5697-5702.

[91] Kim, K. M., Jeong, D. S., Hwang, C. S. 2011. "Nanofilamentary Resistive Switching in Binary Oxide System; a Review on the Present Status and Outlook." *Nanotechnology* 22:254002.

[92] Shuai, Y., Zhou, S., Bürger, D., Helm, M., Schmidt, H. 2011. "Nonvolatile Bipolar Resistive Switching in Au/$BiFeO_3$/Pt." *J. Appl. Phys.* 109:124117.

[93] Janousch, M., Meijer, G. I., Staub, U., Delley, B., Karg, S. F., Andreasson, B. P. 2007. "Role of Oxygen Vacancies in Cr- doped $SrTiO_3$ for Resistance- Change Memory." *Adv. Mater.* 19:2232-2235.

[94] Ohly, C., Hoffmann-Eifert, S., Guo, X., Schubert, J., Waser, R. 2006. "Electrical Conductivity of Epitaxial $SrTiO_3$ Thin Films as a Function of Oxygen Partial Pressure and Temperature." *J. Am. Ceram. Soc.* 89:2845-2852.

[95] Szot, K., Speier, W., Bihlmayer, G., Waser, R. 2006. "Switching the Electrical Resistance of Individual Dislocations in Single-crystalline $SrTiO_3$." *Nat. Mater.* 5:312-320.

[96] Yang, R., Terabe, K., Yao, Y., Tsuruoka, T., Hasegawa, T., Gimzewski, J. K., Aono, M. 2013. "Synaptic Plasticity and Memory Functions Achieved in a WO_{3-x}-based Nanoionics Device by Using the Principle of Atomic Switch Operation." *Nanotechnology* 24:384003.

[97] Kao, K. C. 2004. *Dielectric phenomena in solids*. Cambridge, USA: Academic Press.

[98] Mojarad, S. A., Kwa, K. S. K., Goss, J. P., Zhou, Z., Ponon, N. K., Appleby, D. J. R., Al-Hamadany, R. A. S., Oneill, A. 2012. "A Comprehensive Study on the Leakage Current Mechanisms of Pt/$SrTiO_3$/Pt Capacitor." *J. Appl. Phys.* 111:014503.

[99] Sangwan, V. K., Jariwala, D., Kim, I. S., Chen, K. S., Marks, T. J., Lauhon, L. J., Hersam, M. C. 2015. "Gate-tunable Memristive Phenomena Mediated by Grain Boundaries in Single-layer MoS_2." *Nat. Nanotechnol.* 10:403-406.

[100] Wördenweber, R., Schwarzkopf, J., Hollmann, E., Duk, A., Cai, B., Schmidbauer, M. 2013. "Impact of Compressive In-plane Strain on the Ferroelectric Properties of Epitaxial $NaNbO_3$ Films on (110) $NdGaO_3$." *Appl. Phys. Lett.* 103:132908.

[101] Cai, B., Schwarzkopf, J., Hollmann, E., Braun, D., Schmidbauer, M., Grellmann, T., Wördenweber, R. 2016. "Electronic Characterization

of Polar Nanoregions in Relaxor-type Ferroelectric $NaNbO_3$ Films." *Phys. Rev. B* 93:224107.

[102] Cai, B., Schwarzkopf, J., Feldt, C., Sellmann, J., Markurt, T., Wördenweber, R. 2017. "Combined Impact of Strain and Stoichiometry on the Structural and Ferroelectric Properties of Epitaxially Grown $Na_{1+x}NbO_{3+\delta}$ Films on (110) $NdGaO_3$." *Phys. Rev. B* 95:184108.

[103] Liang, S., Dai, Y., von Helden, L., Schwarzkopf, J., Wördenweber, R. 2018. "Surface Acoustic Waves in Strain-engineered $K_{0.7}Na_{0.3}NbO_3$ Thin Films." *Appl. Phys. Lett.* 113:052901.

[104] von Helden, L., Schmidbauer, M., Liang, S., Hanke, M., Wördenweber, R., Schwarzkopf, J. 2018. "Ferroelectric Monoclinic Phases in Strained $K_{0.7}Na_{0.3}NbO_3$ Thin Films Promoting Selective Surface Acoustic Wave Propagation." *Nanotechnology* 29:415704.